iScience

CellPress

Article

Amphiphilic Oxo-Bridged Ruthenium "Green Dimer" for Water Oxidation

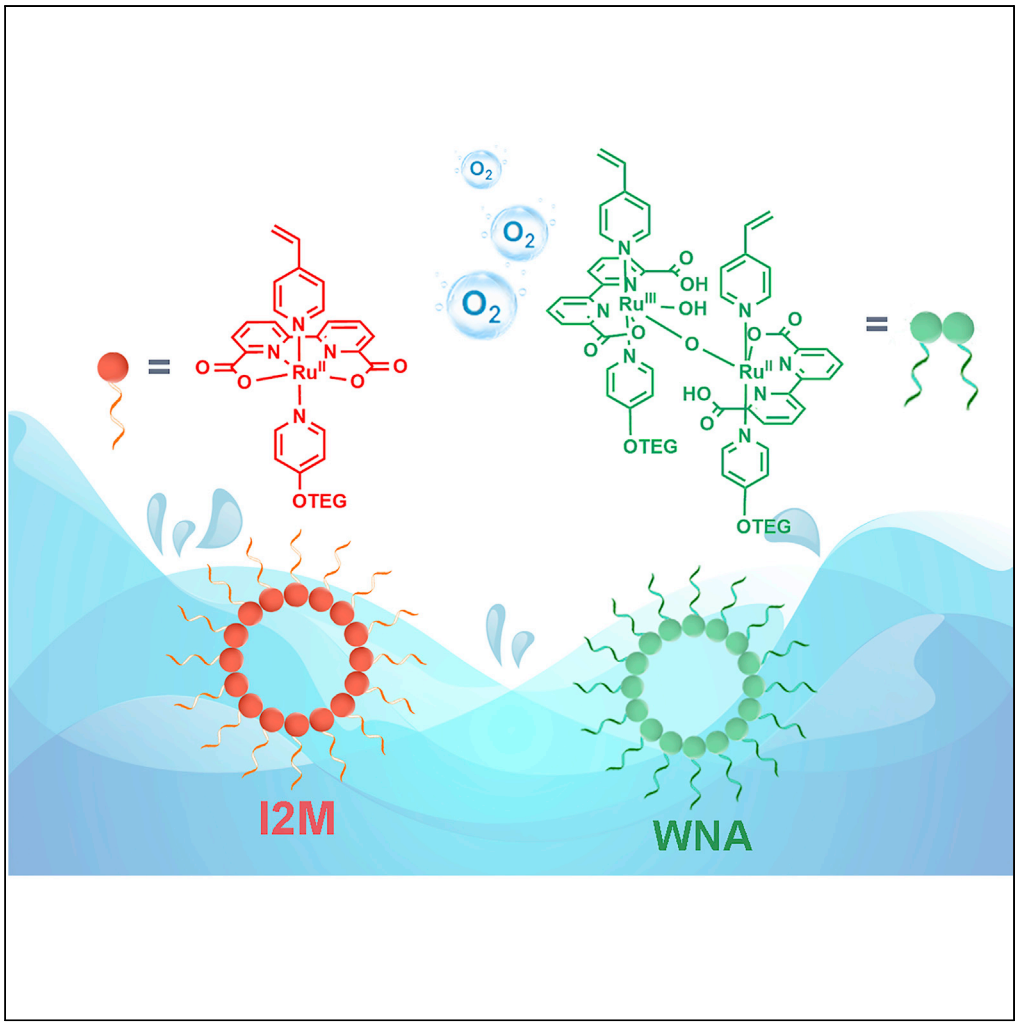

Qing-Qing Yang, Xin Jiang, Bing Yang, Yang Wang, Chen-Ho Tung, Li-Zhu Wu

lzwu@mail.ipc.ac.cn

HIGHLIGHTS

Green dimer (Ru^{II}-O-Ru^{III}), referring to "blue dimer" of Ru^{III}-O-Ru^{III}, is disclosed

The first amphiphilic μ-oxido-bridged catalyst is reported active for water oxidation

The oxo-bridged "green dimer" **2** takes water nucleophilic attack for O-O bond formation

This is the first Ru-bda catalyst, which possesses a new oxygen evolution pathway

Yang et al., iScience *23*, 100969
March 27, 2020 © 2020 The Author(s).
https://doi.org/10.1016/j.isci.2020.100969

iScience

CellPress

Article

Amphiphilic Oxo-Bridged Ruthenium "Green Dimer" for Water Oxidation

Qing-Qing Yang,[1,2] Xin Jiang,[1,2] Bing Yang,[1,2] Yang Wang,[1,2] Chen-Ho Tung,[1,2] and Li-Zhu Wu[1,2,3,*]

SUMMARY

In 1982, an oxo-bridged dinuclear ruthenium(III) complex, known as "blue dimer," was discovered to be active for water oxidation. In this work, a new amphiphilic ruthenium "green dimer" 2, obtained from an amphiphilic mononuclear Ru(bda) (N-OTEG) (L1) (1; N-OTEG = 4-(2-(2-(2-methoxyethoxy) ethoxy)ethoxy)-pyridine; L1 = vinylpyridine) is reported. An array of mechanistic studies identifies "green dimer" 2 as a mixed valence of Ru^{II}-O-Ru^{III} oxo-bridged structure. Bearing the same bda^{2-} and amphiphilic axial ligands, monomer 1 and green dimer 2 can be reversibly converted by ascorbic acid and oxygen, respectively, in aqueous solution. More importantly, the oxo-bridged "green dimer" 2 was found to take water nucleophilic attack for oxygen evolution, in contrast to monomer 1 via radical coupling pathway for O-O bond formation. This is the first report of an amphiphilic oxo-bridged catalyst, which possesses a new oxygen evolution pathway of Ru-bda catalysts.

INTRODUCTION

In natural photosystem II (PSII), a tetra-manganese-calcium molecular cluster (Mn_4CaO_5) serves as the active center to split water for oxygen evolution with generation of four protons and electrons ($2H_2O \rightarrow O_2 + 4H^+ + 4e^-$) (Ferreira et al., 2004; Umena et al., 2011; Yano and Yachandra, 2014; Suga et al., 2019). The astonishing activity and stability of the oxygen evolution complex (OEC-PSII) stimulate the scientific community to develop artificial molecular catalysts that are sufficiently rugged and efficient to remove four electrons and four protons for water oxidation (Concepcion et al., 2009; Inoue et al., 2011; Garrido-Barros et al., 2017). Since the first discovery by Meyer and coworkers that an oxo-bridged dinuclear ruthenium(III) complex Ru^{III}-O-Ru^{III} (Gersten et al., 1982), known as "blue dimer," was active for water oxidation, a large number of molecular catalysts have been identified and considerable knowledge with respect to their activity has been generated (Kärkäs et al., 2014; Blakemore et al., 2015; Zong and Thummel, 2005;Concepcion et al., 2008; Shigeyuki and Ken, 2009; Duan et al., 2009). A survey of these molecular catalysts reported to date revealed that Ru-bda (bda = 2,2′-bipyridine-6,6′-dicarboxylic acid) complex is the most efficient water oxidation catalyst (Duan et al., 2009, 2012), which had been demonstrated to operate O-O bond formation via coupling two oxo-radical (I2M) pathway, rather than via water nucleophilic attack (WNA) pathway (Zhan et al., 2017; Hessels et al., 2017; Xie et al., 2018; Pushkar et al., 2018). From a mononuclear Ru(bda) $(pic)_2$ (pic = 4-picoline), Sun and Sakai independently reported an oxido-bridged trinuclear species Ru^{III}-O-Ru^{IV}-O-Ru^{III} (Zhang et al., 2016; Tsubonouchi et al., 2016). During photocatalytic water oxidation, Sun et al. obtained the trimer under alkaline solution. Sakai et al. suggested that the oxido-bridged trinuclear species obtained *in situ* in the air conditions could serve as an active catalyst for photochemical oxygen evolution. Given that recent reports have renewed interest toward the construction of oxo-bridged water oxidation catalysts (Concepcion et al., 2015; Daniel et al., 2018; Jiang et al., 2018; Lopez et al., 2014), we become particularly interested in designing oxo-bridged molecular catalysts and understanding the cooperative action of substrate water access, proton release, and dioxygen formation in oxo-bridged molecular clusters.

In the present work, we report a new type of oxo-bridged ruthenium catalyst, Ru^{II}-O-Ru^{III} (**2**), formed by air oxidation of designed amphiphilic mono-ruthenium(II) catalyst Ru(bda) (**N-OTEG**) (**L1**) (**1**) (Figures S1–S4). The color of monomer **1** in aerobic aqueous solution gradually changed from red to green as shown in Figure 1. Studies using mass spectrometry (MS), nuclear magnetic resonance (NMR), Raman spectrum, UV visible spectroscopy (UV-vis), electron paramagnetic resonance (EPR), and X-ray absorption near edge structure (XANES) identified that green species from **1** is a more stable oxo-bridged dinuclear structure of Ru^{II}-O-Ru^{III} (**2**). More importantly, "green dimer" **2** is catalytically active with a surprising mechanism change for O-O bond formation from radical coupling pathway for monomer **1** to water nucleophilic attack pathway.

[1]Key Laboratory of Photochemical Conversion and Optoelectronic Materials, Technical Institute of Physics and Chemistry, The Chinese Academy of Sciences, Beijing 100190, P. R. China

[2]School of Future Technology, University of Chinese Academy of Sciences, Beijing 100190, P. R. China

[3]Lead Contact

*Correspondence: lzwu@mail.ipc.ac.cn

https://doi.org/10.1016/j.isci.2020.100969

This is an open access article under the CC BY-NC-ND license (http://creativecommons.org/licenses/by-nc-nd/4.0/).

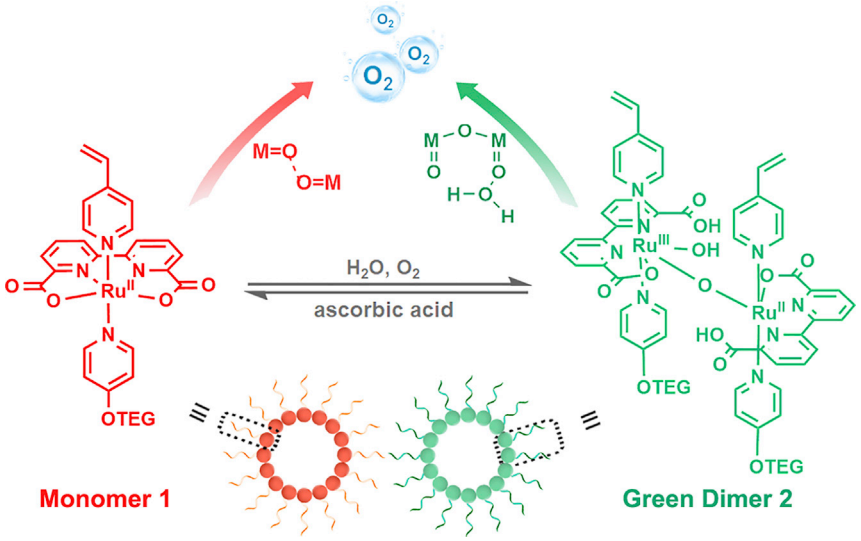

Figure 1. Monomer 1 and Green Dimer 2

RESULTS AND DISCUSSION

Amphiphilic monomer **1**, containing hydrophilic ether chain and vinylpyridine as axial ligands and bda^{2-} segment as equatorial ligand, was synthesized by a two-step reaction (Duan et al., 2009). UV-vis spectra of monomer **1** in aerobic aqueous solution showed a decrease of metal-to-ligand charge transfer absorption bands from 350 nm to 550 nm and an increase at 695 nm along with time (Figure 2B). The solution of **1** turned from red to green within several hours in aerobic aqueous solution (Figure 2A), but no change was observed in water under nitrogen atmosphere (Figure S8). To identify the new species, we refluxed **1** with water under air for 24 h. The obtained green species exhibited a new signal of *m/z* at 1,416.22, which is in agreement with a Ru-O-Ru structure of (**2**, Calcd, 1,416.25). The experimental isotopic peak of ESI-MS spectrum was consistent with the simulation results (Figures S5 and S6). Considering that Sakai and Sun assigned a similar absorption band at ~690 nm in the oxido-bridged trinuclear species Ru^{III}-O-Ru^{IV}-O-Ru^{III} to intervalence charge transfer absorption of $Ru^{III} \rightarrow Ru^{IV}$ in buffer solution (Zhang et al., 2016; Tsubonouchi et al., 2016), we tentatively attributed the absorption at 695 nm in our case to intervalence charge transfer character in water. With addition of ascorbic acid from 0.1 equivalent to 1.0 equivalent (as the manner of the concentration of Ru center) to the solution, the 695 nm peak intensity of **2** decreased and kept constant with further addition of ascorbic acid (Figure 2C). Upon exposure to air, however, the absorption at 695 nm gradually emerged (Figures 2A and S12). The fact that the same ESI-MS signal at 691.13 as that of monomer **1** was detected for the reduced system of **2** (Figure S7) suggested that green dimer **2** can be easily synthesized by oxidation of monomer **1** with oxygen and returned to **1** by ascorbic acid in water.

Amphiphiles with hydrophilic and hydrophobic moieties are capable of self-assembling in solutions or at interfaces, thus enabling **1** and **2** water soluble (Yang et al., 2016). Dynamic light scattering (DLS) measurements showed that monomer **1** and dimer **2** aggregated in water to form assemblies with diameters around 50 nm (see Table S2), in accordance with scanning electron microscope (SEM) images (Figure S13). The UV-vis absorption spectra of different concentrations of monomer **1** blue shifted in water, consistent with the aggregation behaviors (Figure S14). To determine the critical aggregation concentration (CAC) of monomer **1** and dimer **2**, organic dye Nile red was selected (Yang et al., 2016). When the concentration is higher than the CAC, Nile red would like to go inside the aggregates to show strong fluorescence, whereas Nile red shows no absorption and fluorescence in water. From the triggered strong fluorescence of Nile red even at a low concentration of monomer **1** and dimer **2** (Figures S15–S17), we inferred that both **1** and **2** at the catalytic concentration has existed as the aggregation forms in water. Possible due to the amphiphilic self-assembly, crystal structures of monomer **1** and dimer **2** as well as multi-core Ru-bda structure of Ru^{III}-O-Ru^{IV}-O-Ru^{III} reported in literature (Zhang et al., 2016; Tsubonouchi et al., 2016) were not obtained.

To shed more light on the structure of **2**, Raman spectra of **1** and **2** were examined by 532 nm and 633 nm excitations, which are close to the maximal absorption band to have Raman spectrum with high intensity.

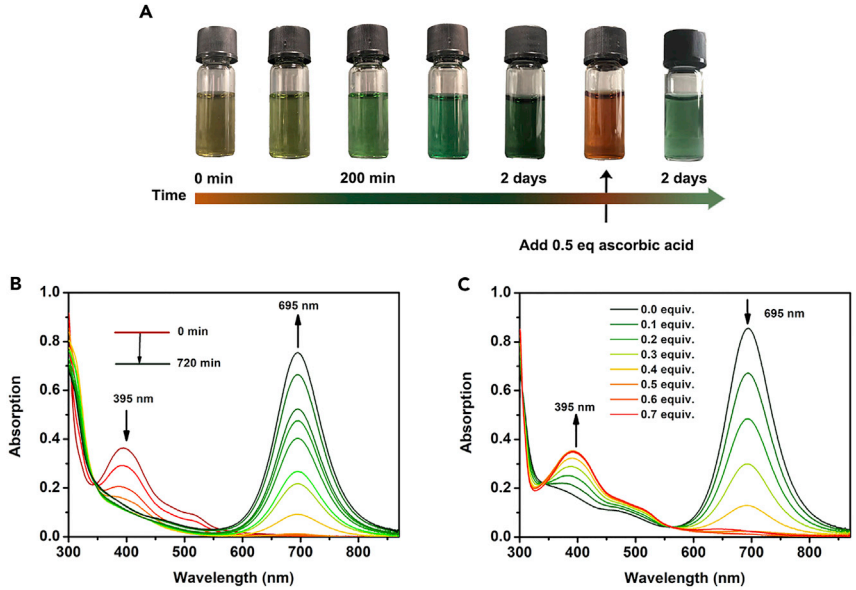

Figure 2. The Transition of Monomer 1 and Green Dimer 2

(A) The solution color change of **1** (1.0×10^{-3} M) from left to right in an oxygen saturated aqueous solution over time.

(B) UV-vis spectral changes of **1** (2.0×10^{-5} M) in an oxygen saturated aqueous solution along with time.

(C) UV-vis spectral of **2** (1.0×10^{-5} M) after addition of 0–1.0 equivalent ascorbic acid (as the manner of the concentration of Ru center) in water.

In the 150–1,500 cm^{-1} region, the spectrum of **1** in $H_2{}^{16}O$ was dominated by the intense absorption bands near 500 cm^{-1}, 700 cm^{-1}, and 1,500 cm^{-1} (Figure S18). Above 1,000 cm^{-1}, a series of bands of **1** arises from ring vibrations of the bda^{2-} and substituted pyridine ligand. Treatment of **1** with $^{16}O_2$ in $H_2{}^{16}O$ to synthesize **2** showed a new band at 374 cm^{-1}, 462 cm^{-1}, and 785 cm^{-1}, which was tentatively assigned to the symmetric Ru-^{16}O-Ru stretches of the bridge, ν_{sym} (Ru-^{16}O-Ru) (Jurss et al., 2012; Moonshiram et al., 2012), whereas the bands above 1,000 cm^{-1} were weak in a relative sense. When green dimer **2** was generated from the aerobic solution of $H_2{}^{18}O$ with $^{16}O_2$, the 374 cm^{-1}, 462 cm^{-1}, and 785 cm^{-1}, bands of ν_{sym} (Ru-O-Ru) shifted to 359 cm^{-1}, 409 cm^{-1}, and 741 cm^{-1} corresponding to the isotopic shift value (see Table S3) (Polyansky et al., 2011). When green dimer **2** was obtained from **1** in $H_2{}^{16}O$ under $^{18}O_2$ atmosphere, the slight shifts to 369 cm^{-1}, 430 cm^{-1}, and 771 cm^{-1} indicated that oxygen atom of the oxo-bridge Ru-O-Ru is dominantly from H_2O with interference of O_2 (Wilson and Jain, 2018; Moonshiram et al., 2016).

X-ray absorption near edge structure (XANES), powerful in monitoring the valence state of metal complexes, was performed to affirm the valence state of monomer **1** and dimer **2** (Moonshiram et al., 2012; Pushkar et al., 2014; Yang et al., 2017; Lebedev et al., 2017). As shown in Figure 3A, the absorption edge of the Ru metal center of **2** shifted to a higher energy at 22,129.0 eV, indicating an increase in the average valence of Ru center in **2**. Adding 1.0 equivalent ascorbic acid (as the manner of the concentration of **2**) to green dimer **2** aqueous solution returned the K-edge shift to the initial state at 22,127.9 eV of Ru^{II}. The derivative K-edges of Ru(bda) $(pic)_2$, $RuCl_3$, RuO_2, monomer **1**, dimer **2**, and dimer **2** reduced by 1.0 equivalent ascorbic acid (relative to the concentration of **2**) are shown in Figures S19 and S20 and Table S4. Each of the standard samples has an ~1 eV difference, so do monomer **1** and dimer **2**. Besides, EPR experiment was consistent with the expected Ru^{II} state of monomer **1** (Figure S26). A solution of **1** under argon atmosphere was EPR-silent, whereas green dimer **2** showed a signal at g = 2.46 and 2.33 corresponding to the Ru^{III} species (Pushkar et al., 2014; Murakami et al., 2011). After adding 1.0 equivalent ascorbic acid to the solution of dimer **2**, the Ru^{III} species of **2** was reduced to return EPR silent form.

By simulation of the multiple scattering paths from the crystal coordinates of Ru(bda) $(pic)_2$ (Duan et al., 2009) and $\{[Ru^{III}(bda)\text{-}(pic)_2(m\text{-}O)]_2Ru^{IV}(pic)_2(H_2O)_2\}^{2+}$ (Tsubonouchi et al., 2016), the molecular structure and ligand environment of metal center in monomer **1** and dimer **2** were further analyzed by extended X-ray absorption fine structure (EXAFS) (Figure 3B) (Creus et al., 2016; Lebedev et al., 2017; Moonshiram

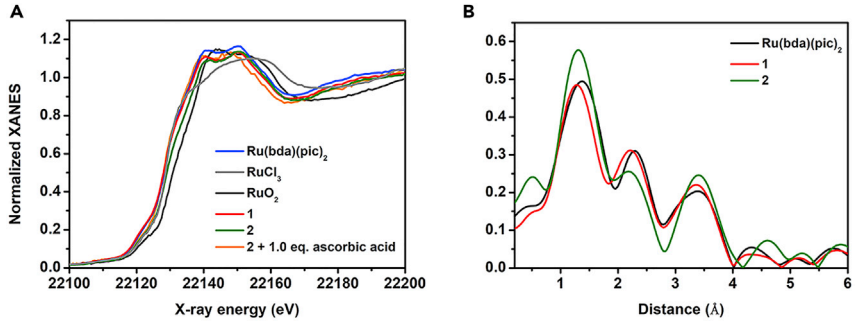

Figure 3. The Valence State of Monomer 1, Dimer 2, and Standard Samples by X-Ray Absorption Spectroscopic Observation

(A) Normalized Ru K-edge XANES of **1**, **2**, and **2** (5.0×10^{-3} M) reduced with 1.0 equiv. (as the manner of the concentration of **2**) ascorbic acid in water. The powder of ruthenium was used as the standard sample of Ru(bda) $(pic)_2$; $RuCl_3$ and RuO_2 were showed in company as standard sample of Ru^{II}, Ru^{III}, and Ru^{IV}, respectively.

(B) Corresponding k^3-weighted Fourier transform (FT) of Ru EXAFS of Ru(bda) $(pic)_2$ (powder), **1** and **2** (5.0×10^{-3} M).

et al., 2012, 2016). The resulting Ru-N and Ru-O distances of Ru(bda) $(pic)_2$, monomer **1**, and dimer **2** are in a good agreement with the average Ru-N and Ru-O distances of the first coordination shell. As shown in Figures S21–S23 and Table S5, the fitting Ru-N distance of 1.91 Å and Ru-O distance of 2.06 Å in monomer **1** are in line with the average Ru-N and Ru-O distance in crystallographic Ru(bda) $(pic)_2$. Analysis of dimer **2** referring to $\{[Ru^{III}(bda)\text{-}(pic)_2(m\text{-}O)]_2Ru^{IV}(pic)_2(H_2O)_2\}^{2+}$ (Tsubonouchi et al., 2016) resolved Ru-N interaction at 1.97 Å, a larger Ru-O distance at 2.13 Å and a Ru-O-Ru distance at 3.51 Å (Tables S5 and Figure S24). The strong peak at 3.51 Å for Ru(bda) $(pic)_2$ and monomer **1** was assigned to 10 forward triangle scattering paths of Ru-C. One Ru-O-Ru forward triangle scattering path, together with another 10 forward triangle scattering paths of Ru-C, was involved to fit EXAFS data of dimer **2**. Due to the increased coordination numbers (Zhang, 2014), the intensity of dimer **2** at ~1.5 and ~3.5 Å was increased. The distance above 3 Å corresponding to the distance of Ru-O-Ru originated from the Ru-Ru interaction across the μ-oxo bridge.

A notable oxygen evolution was observed when the water oxidation by amphiphilic monomer **1** and green dimer **2** was performed at room temperature using the water displacement method with $Ce(NH_4)_2(NO_3)_6$ (CAN) as the sacrificial electron acceptor at pH 2.0. All the solutions were degassed by nitrogen before use. Monomer **1** and green dimer **2** have good stabilities in water under nitrogen atmosphere (Figures S8 and S9). When adding monomer **1** (7.0×10^{-5} M) into a solution of 0.5 M CAN (Figure S25), more than 2,300 equivalent molecular oxygen was obtained (turnover number(TON) of 2,302). Under the same condition, oxygen was released by dimer **2** (7.0×10^{-5} M) with a TON of 2,608 (as the manner of the concentration of **2**). Clearly, the formation of the Ru^{II}-O-Ru^{III} structure with a μ-oxido bridge is an active species for water oxidation. To clarify the oxygen source of **1** and **2**, we conducted the mass spectrometric analysis of the evolved O_2 using 97% $H_2{}^{18}O$ as solution (Murakami et al., 2011). The molecular ion peak at m/z = 36 assignable to $^{18}O_2$ exhibited the largest intensity of 89.17% for monomer **1** and 91.24% for dimer **2** among molecular ion peaks at m/z = 32, 34, and 36 (Table S6). The observed ratios of **1** and **2** agreed well with the calculated ratios, indicating that the oxygen atom in the bridge of Ru^{II}-O-Ru^{III} **2** did not involve in the O-O bond formation. Furthermore, the water-oxidation kinetics as a function of concentration was investigated by Clark oxygen electrode. The fastest oxygen evolution time period of 10 s was chosen to avoid the conversion of monomer **1** to green dimer **2** during the reaction time. As shown in Figures 4A and 4C, catalyst **1** had a linear fitting correlation (R^2 = 0.99) between concentration square and initial rate, indicating the radical coupling mechanism (I2M) for O-O bond formation (Wang et al., 2012; Yang et al., 2016). However, green dimer **2**, plotting against the initial rate of oxygen evolution, suggested a water nucleophilic attack pathway (WNA) in the rate-determining step of O-O bond formation (Figures 4B and 4D). Surprisingly, the O-O bond formation pathways altered from radical coupling pathway to water nucleophilic attack when monomer **1** was replaced by dimer **2**. The kinetic isotope effect (KIE) of **1** at different concentration was calculated as 1.19, in agreement with the previously established radical coupling pathway for O-O bond formation of Ru(bda) catalysts (Figure 4C), whereas the O-O bond formation of **2** with a KIE of 2.18 (Figure 4D) is similar to the famous blue dimer for O-O bond

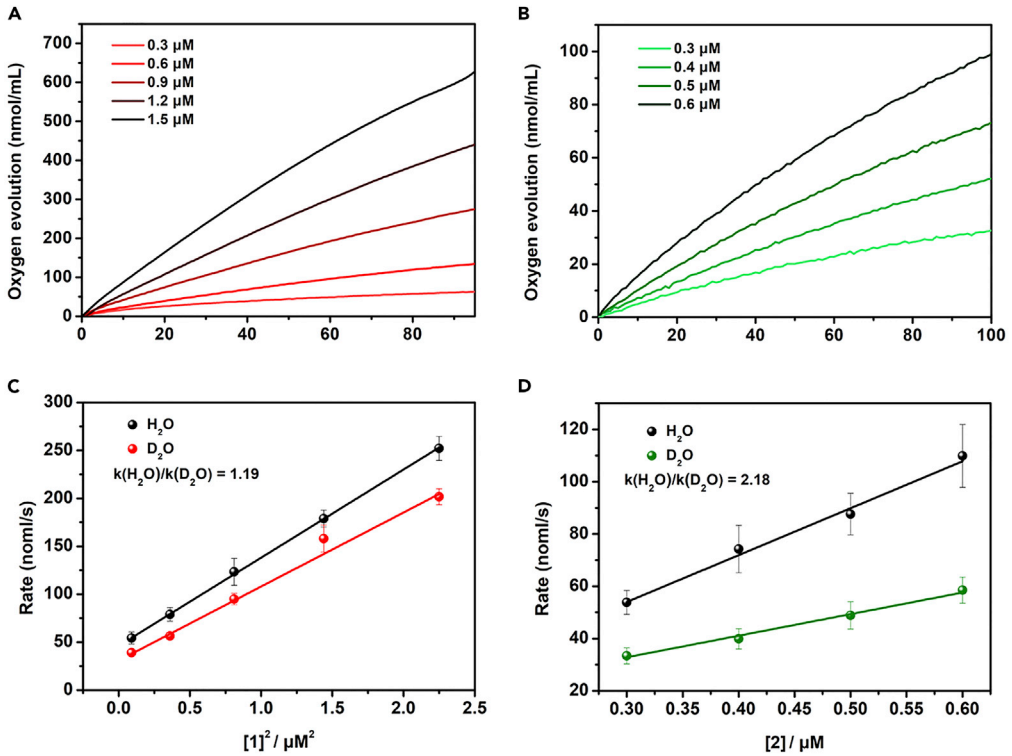

Figure 4. The Kinetic Study of Monomer 1 and Dimer 2 for Water Oxidation

Oxygen evolution of monomer **1** (A) and dimer **2** (B) as a function of concentration (0.3–1.5×10^{-6} M) in water.The plots of the initial oxygen evolution rate in the first 10 s reaction system of **1** (C) and **2** (D) in H_2O and D_2O, respectively. The average k values from three sets were used to obtain KIE value.

formation via water nucleophilic attack (Schulze et al., 2016; Shaffer et al., 2016; Khan et al., 2015; Yu et al., 2018).

When 1.0 equivalent CAN was added to the system of **1**, an EPR signal at g = 2.30, 2.19 and 1.82 character showed up (Figure S27). Further addition of 3.0 equivalent CAN caused a new signal at g = 2.28, 2.09, and 1.85. These EPR signals of monomer **1** fit quite well with that reported in literature for Ru^{III} and Ru^{V} species (Pushkar et al., 2014; Erdman et al., 2017; Pineda-Galvan et al., 2019). With 1.0 equivalents of CAN, dimer **2** showed a signal at g = 2.28, 2.16, 1.84 of Ru^{III} species (Figure S28). However, the poor signals for dimer **2** with 5.0 equivalents of CAN deterred us from immediately attributing these peaks to Ru^{V} species. Additionally, spectroelectrochemistry was carried out. With increasing the potential from 0 to 1.3 V vs. SCE (Figures S29 and S30), the metal-to-ligand charge transfer (MLCT) absorption bands of monomer **1** at 395 nm and 520 nm decreased along with the consumption of Ru^{II} species, whereas the intervalence charge transfer absorption bands of dimer **2** decreased at 695 nm accompanying with an increase at 445 nm that is consistent with the conversion of [Ru^{II}-O-Ru^{III}→ Ru^{III}-O-Ru^{III}] process.

To further understand the electron and proton release processes for water oxidation, differential pulse voltammograms (DPV) of monomer **1** and dimer **2** were studied (Figures S31–S34). Three oxidation peaks in the DPV curve of monomer **1** were observed at 446, 826, and 1022 mV versus SCE (saturated calomel electrode) at pH 2.0, which was assigned to [Ru^{II}→Ru^{III}],[Ru^{III}→Ru^{IV}] and [Ru^{IV}→Ru^{V}] couples, respectively (Figure S31). The DPV curve of green dimer **2** showed five oxidation peaks at 132; 470; 808; 1,039; and 1,280 mV vs SCE corresponding to the five oxidation processes of **2** as [Ru^{II}-O-Ru^{III}→Ru^{III}-O-Ru^{III}], [Ru^{III}-O-Ru^{III}→Ru^{III}-O-Ru^{IV}], [Ru^{III}-O-Ru^{IV}→Ru^{IV}-O-Ru^{IV}], [Ru^{IV}-O-Ru^{IV}→Ru^{V}-O-Ru^{IV}], and [Ru^{V}-O-Ru^{IV}→Ru^{V}-O-Ru^{V}], respectively. From the Pourbaix diagram of **1** within the arrangement of pH 1–4, the [Ru^{II}→Ru^{III}] couple is pH-independent, whereas the [Ru^{III}→Ru^{IV}] and the [Ru^{IV}→Ru^{V}] processes have the slopes of 58 mV/pH and 61 mV/pH, respectively (Figures 5A and S33), indicating an $1e^{-}/1H^{+}$ process (Wasylenko et al., 2010; Murakami et al., 2011). Thus, the three oxidation processes of monomer **1** at pH 2.0 are

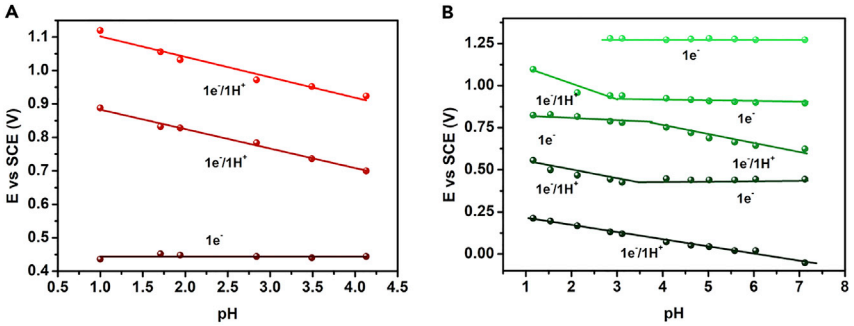

Figure 5. Investigation of the Electron and Proton Transfer Processes of Monomer 1 and Dimer 2

Pourbiax diagram of **1** (A) and **2** (B) (1.0×10^{-3} M) in a solution of 0.1 M Na_2SO_4 using HNO_3-NaOH to adjust the pH values. Conditions: glassy carbon as working electrode, Pt wire as auxiliary electrode, and saturated calomel electrode as reference electrode.

[Ru^{II}-OH_2 → Ru^{III}-OH_2], [Ru^{III}-OH_2 → Ru^{IV}-OH], and [Ru^{IV}-OH → Ru^{V}=O]. As for the electron and proton transfer of mixed-valence dimer **2** during water oxidation by CAN at pH 2.0, the three processes of [Ru^{II}-O-Ru^{III} → Ru^{III}-O-Ru^{III}], [Ru^{III}-O-Ru^{III} → Ru^{III}-O-Ru^{IV}], and [Ru^{IV}-O-Ru^{IV} → Ru^{V}-O-Ru^{IV}] involved an $1e^-/1H^+$ process, whereas the [Ru^{III}-O-Ru^{IV} → Ru^{IV}-O-Ru^{IV}] and [Ru^{V}-O-Ru^{IV} → Ru^{V}-O-Ru^{V}] processes were pH independent (Figures 5B and S34). Therefore, the water oxidation processes of dimer **2** could be summarized as [OH_2-Ru^{II}-O-Ru^{III}-OH → OH-Ru^{III}-O-Ru^{III}-OH], [OH-Ru^{II}-O-Ru^{III}-OH → O=Ru^{IV}-O-Ru^{III}-OH], [O=Ru^{IV}-O-Ru^{III}-OH → O=Ru^{IV}-O-Ru^{IV}-OH], [O=Ru^{IV}-O-Ru^{IV}-OH → O=Ru^{V}-O-Ru^{IV}= O], and [O=Ru^{IV}-O-Ru^{IV}=O → O=Ru^{V}-O-Ru^{V}=O], respectively.

Combined with all above experimental results, the oxygen evolution of the whole catalytic cycles of monomer **1** and green dimer **2** could be summarized as follows (Figure 6). Amphiphilic mononuclear **1** could form an intermediate of Ru^{III}-H_2O with the supplementary oxidation by oxygen and then react with another molecule of **1** to generate "green dimer" **2**. In the presence of CAN, monomer **1** performed a radical coupling pathway by Ru^{V}=O intermediate; however, dimer **2** with the Ru^{II}-O-Ru^{III} structure operated a water nucleophilic attack pathway to form the O-O bond (Concepcion et al., 2015; Moonshiram et al., 2013). The μ-oxido bridge of dimer **2** may prevent the coupling from two high Ru^{V}=O species, thus resulting in water nucleophilic attack pathway to generation of oxygen. The alternation of the catalytic pathway for oxygen evolution leads to different water oxidation performance of the amphiphilic Ru-bda monomer **1** and its oxido-bridged green dimer **2**.

In summary, we report an amphiphilic oxo-bridged dimer catalyst **2** for the first time for water oxidation, which is easily generated by monomer **1** in aerobic aqueous solution. With detailed characterization and analysis, the structure of green dimer **2** has been identified as a Ru^{II}-O-Ru^{III} oxo-bridged mixed-valence species, referring to the famous "blue dimer" of Ru^{III}-O-Ru^{III}. The amphiphilic monomer **1** and green dimer **2** can catalyze water oxidation for oxygen evolution in high efficiency. The presence of μ-oxido-bridge greatly influences the catalytic behavior on O-O bond formation for Ru-bda catalysts in water. A mechanistic change of O-O bond formation from radical coupling pathway to water nucleophilic attack reveals another important oxygen evolution pathway of Ru-bda catalysts. The conversion of monomer **1** to oxo-bridged dimer **2** may signify that the real form of the long-lived Ru-bda catalysts would be close to the nature's mastery of the multinuclear structure of Mn_4CaO_5 with μ-oxido bridges.

Limitations of the Study

Our results show that an amphiphilic μ-oxido-bridged catalyst is active for water oxidation for the first time. Referring to the famous "blue dimer" of Ru^{III}-O-Ru^{III}, green dimer (Ru^{II}-O-Ru^{III}) (**2**) formed by air oxidation of amphiphilic mono-ruthenium(II) catalyst Ru(bda) (**N-OTEG**) (**L1**) (**1**), has been demonstrated to take water nucleophilic attack for oxygen evolution, which is distinct from monomer **1** via radical coupling pathway for O-O bond formation. Further investigation with advanced *in-situ* techniques may provide a deeper insight on the high-valence catalytic intermediates that may give more enlightenment to design more robust molecular catalysts for water oxidation.

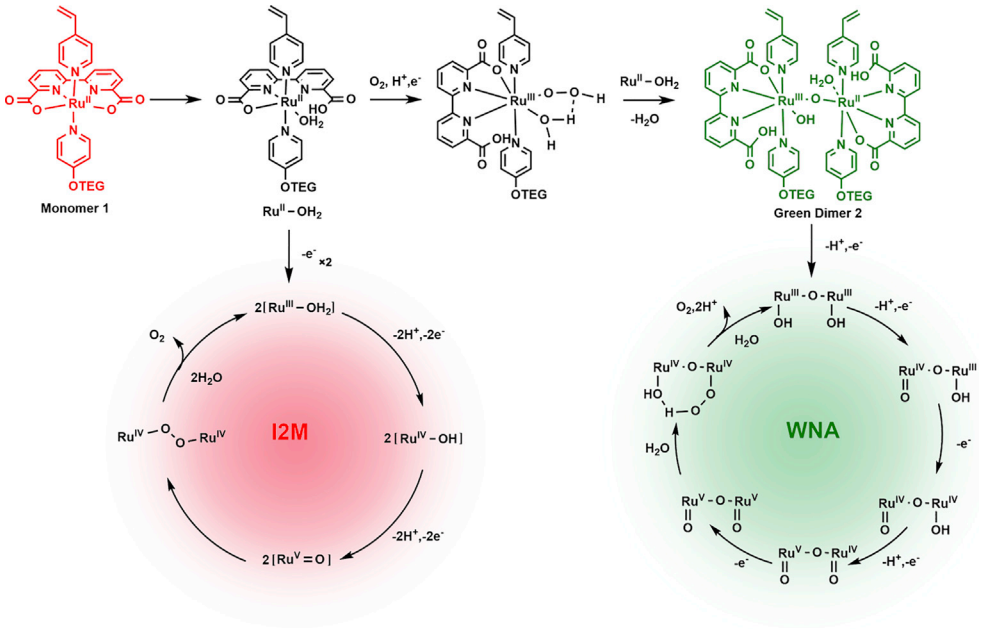

Figure 6. Proposed mechanism for water oxidation catalyzed by monomer 1 and dimer 2 in water.

METHODS

All methods can be found in the accompanying Transparent Methods supplemental file.

DATA AND CODE AVAILABILITY

Raw data and code used to produce Figures 2, 3, 4, 5, and Figures S1–S34 are available upon reasonable request to the corresponding authors.

SUPPLEMENTAL INFORMATION

Supplemental Information can be found online at https://doi.org/10.1016/j.isci.2020.100969.

ACKNOWLEDGMENTS

We are grateful for financial support from the Ministry of Science and Technology of the People's Republic of China (2017YFA0206903), the National Natural Science Foundation of China (21861132004), the Strategic Priority Research Program of the Chinese Academy of Science (XDB17000000), Key Research Program of Frontier Sciences of the Chinese Academy of Science (QYZDY-SSW-JSC029), and K. C.Wong Education Foundation.

AUTHOR CONTRIBUTIONS

L.-Z.W. devised the initial concept for the work. Q.-Q.Y. and X.-J. contributed to the synthesis of products and mechanism investigation. W.Y. performed EXAFS fitting data. J.X., B.Y., and C.-H.T. helped with the discussion and analysis of the data. L.-Z.W. and Q.-Q.Y. wrote the manuscript.

DECLARATION OF INTERESTS

The authors declare no competing interests.

Received: November 13, 2019
Revised: January 27, 2020
Accepted: March 4, 2020
Published: March 27, 2020

REFERENCES

Blakemore, J.D., Crabtree, R.H., and Brudvig, G.W. (2015). Molecular catalysts for water oxidation. Chem. Rev. *115*, 12974–13005.

Concepcion, J.J., Jurss, J.W., Brennaman, M.K., Hoertz, P.G., Patrocinio, A.O.T., Iha, N.Y.M., Templeton, J.L., and Meyer, T.J. (2009). Making oxygen with Ruthenium complexes. Acc. Chem. Res. *42*, 1954.

Concepcion, J.J., Jurss, J.W., Templeton, J.L., and Meyer, T.J. (2008). One site is enough. catalytic water oxidation by $[Ru(tpy)(bpm)(OH_2)]^{2+}$ and $[Ru(tpy)(bpz)(OH_2)]^{2+}$. J. Am. Chem. Soc. *130*, 16462–16463.

Concepcion, J.J., Zhong, D.K., Szalda, D.J., Muckerman, J.T., and Fujita, E. (2015). Mechanism of water oxidation by $[Ru(bda)(L)_2]$: the return of the "blue dimer". Chem. Commun.(Camb.) *51*, 4105–4108.

Creus, J., Matheu, R., Peñafiel, I., Moonshiram, D., Blondeau, P., Benet-Buchholz, J., García-Antón, J., Sala, X., Godard, C., and Llobet, A. (2016). A million turnover molecular anode for catalytic water oxidation. Angew. Chem. Int. Ed. *55*, 15382–15386.

Daniel, Q., Duan, L., Timmer, B.J.J., Chen, H., Luo, X., Ambre, R., Wang, Y., Zhang, B., Zhang, P., Wang, L., et al. (2018). Water oxidation initiated by *in situ* dimerization of the molecularRu(pdc) catalyst. ACS Catal. *8*, 4375–4382.

Duan, L., Bozoglian, F., Mandal, S., Stewart, B., Privalov, T., Llobet, A., and Sun, L. (2012). A molecular ruthenium catalyst with water-oxidation activity comparable to that of photosystem II. Nat. Chem. *4*, 418–423.

Duan, L., Fischer, A., Xu, Y., and Sun, L. (2009). Isolated seven-coordinate Ru(IV) dimer complex with $[HOHOH]^-$ bridging ligand as an intermediate for catalytic water oxidation. J. Am. Chem. Soc. *131*, 10397–10399.

Erdman, D., Pineda-Galvan, Y., and Pushkar, Y. (2017). Mechanistic analysis of water oxidation catalyst cis-$[Ru(bpy)_2(H_2O)_2]^{2+}$: effect of dimerization. Catalysts *7*, 39.

Ferreira, K.N., Iverson, T.M., Maghlaoui, K., Barber, J., and Iwata, S. (2004). Architecture of the photosynthetic oxygen-evolving center. Science *303*, 1831–1838.

Garrido-Barros, P., Gimbert-Suriñach, C., Matheu, R., Sala, X., and Llobet, A. (2017). How to make an efficient and robust molecular catalyst for water oxidation. Chem. Soc. Rev. *46*, 6088–6098.

Gersten, S.W., Samuels, G.J., and Meyer, T.J. (1982). Catalytic oxidation of water by an oxo-bridged ruthenium dimer. J. Am. Chem. Soc. *104*, 4029–4030.

Hessels, J., Detz, R.J., Koper, M.T.M., and Reek, J.N.H. (2017). Rational design rules for molecular water oxidation catalysts based on scaling relationships. Chem. Eur. J. *23*, 16413–16418.

Inoue, H., Shimada, T., Kou, Y., Nabetani, Y., Masui, D., Takagi, S., and Tachibana, H. (2011). The water oxidation bottleneck in artificial photosynthesis: how can we get through it? An alternative route involving a two-electron process. ChemSusChem *4*, 173–179.

Jiang, X., Li, J., Yang, B., Wei, X.-Z., Dong, B.-W., Kao, Y., Huang, M.-Y., Tung, C.-H., and Wu, L.-Z. (2018). A bio-inspired Cu_4O_4cubane: effective molecular catalysts for electrocatalytic water oxidation in aqueous solution. Angew.Chem. Int. Ed. *57*, 7850–7854.

Jurss, J.W., Concepcion, J.J., Butler, J.M., Omberg, K.M., Baraldo, L.M., Thompson, D.G., Lebeau, E.L., Hornstein, B., Schoonover, J.R., Jude, H., et al. (2012). Electronic structure of the water oxidation catalyst cis,cis-$[(bpy)_2(H_2O)Ru^{III}ORu^{III}(OH_2)(bpy)_2]^{4+}$, the blue dimer. Inorg. Chem. *51*, 1345–1358.

Kärkäs, M.D., Verho, O., Johnston, E.V., and Åkermark, B. (2014). Artificial photosynthesis: molecular systems for catalytic water oxidation. Chem. Rev. *114*, 11863–12001.

Khan, S., Yang, K.R., Ertem, M.Z., Batista, V.S., and Brudvig, G.W. (2015). Mechanism of manganese-catalyzed oxygen evolution from experimental and theoretical analyses of ^{18}O kinetic isotope effects. ACS Catal. *5*, 7104–7113.

Lebedev, D., Pineda-Galvan, Y., Tokimaru, Y., Fedorov, A., Kaeffer, N., Copéret, C., and Pushkar, Y. (2017). The key Ru^V=O intermediate of site-isolated mononuclear water oxidation catalyst detected by *in situ* X-ray absorption spectroscopy. J. Am. Chem. Soc. *140*, 451–458.

Lopez, I., Ertem, M.Z., Maji, S., Benet-Buchholz, J., Keidel, A., Kuhlmann, U., Hildebrandt, P., Cramer, C.J., Batista, V.S., and Llobet, A. (2014). A self-improved water-oxidation catalyst: is one site really enough? Angew. Chem. Int. Ed. *53*, 205–209.

Moonshiram, D., Alperovich, I., Concepcion, J.J., Meyer, T.J., and Pushkar, Y. (2013). Experimental demonstration of radicaloid character in a Ru(V)=O intermediate in catalytic water oxidation. Proc.Natl.Acad.Sci. U S A *110*, 3765–3770.

Moonshiram, D., Jurss, J.W., Concepcion, J.J., Zakharova, T., Alperovich, I., Meyer, T.J., and Pushkar, Y. (2012). Structure and electronic configurations of the intermediates of water oxidation in blue Ruthenium dimer catalysis. J. Am. Chem. Soc. *134*, 4625–4636.

Moonshiram, D., Pineda-Galvan, Y., Erdman, D., Palenik, M., Zong, R., Thummel, R., and Pushkar, Y. (2016). Uncovering the role of oxygen atom transfer in Ru-based catalytic water oxidation. J. Am. Chem. Soc. *138*, 15605–15616.

Murakami, M., Hong, D., Suenobu, T., Yamaguchi, S., Ogura, T., and Fukuzumi, S. (2011). Catalytic mechanism of water oxidation with single-site ruthenium-heteropolytungstate complexes. J. Am. Chem. Soc. *133*, 11605–11613.

Pineda-Galvan, Y., Ravari, A.K., Shmakov, S., Lifshits, L., Kaveevivitchai, N., Thummel, R., and Pushkar, Y. (2019). Detection of the site protected 7-coordinate Ru^V=O species and its chemical reactivity to enable catalytic water oxidation. J. Catal. *375*, 1–7.

Polyansky, D.E., Muckerman, J.T., Rochford, J., Zong, R., Thummel, R.P., and Fujita, E. (2011). Water oxidation by a mononuclear ruthenium catalyst: characterization of the intermediates. J. Am. Chem. Soc. *133*, 14649–14665.

Pushkar, Y., Moonshiram, D., Purohit, V., Yan, L., and Alperovich, I. (2014). Spectroscopic analysis of catalytic water oxidation by $[Ru^{II}(bpy)(tpy)H_2O]^{2+}$ suggests that Ru^V=O is not a rate-limiting intermediate. J. Am. Chem. Soc. *136*, 11938–11945.

Pushkar, Y., Pineda-Galvan, Y., Ravari, A.K., Otroshchenko, T., and Hartzler, D.A. (2018). Mechanism for O–O bond formation via radical coupling of metal and ligand based radicals: a new pathway. J. Am. Chem. Soc. *140*, 13538–13541.

Schulze, M., Kunz, V., Frischmann, P.D., and Würthner, F. (2016). A supramolecular ruthenium macrocycle with high catalytic activity for water oxidation that mechanistically mimics photosystem II. Nat. Chem. *8*, 576–583.

Shaffer, D.W., Xie, Y., Szalda, D.J., and Concepcion, J.J. (2016). Manipulating the rate-limiting step in water oxidation catalysis by ruthenium bipyridine-dicarboxylate complexes. Inorg. Chem. *55*, 12024–12035.

Shigeyuki, M., and Ken, S. (2009). Clear evidence showing the robustness of a highly active oxygen-evolving mononuclear Ruthenium complex with an aqua ligand. Chem. Lett. *38*, 182–183.

Suga, M., Akita, F., Yamashita, K., Nakajima, Y., Ueno, G., Li, H., Yamane, T., Hirata, K., Umena, Y., Yonekura, S., et al. (2019). An oxyl/oxo mechanism for oxygen-oxygen coupling in PSII revealed by an x-ray free-electron laser. Science *366*, 334–338.

Tsubonouchi, Y., Lin, S., Parent, A.R., Brudvig, G.W., and Sakai, K. (2016). Light-induced water oxidation catalyzed by an oxido-bridged triruthenium complex with a Ru-O-Ru-O-Ru motif. Chem. Commun.(Camb.) *52*, 8018–8021.

Umena, Y., Kawakami, K., Shen, J.-R., and Kamiya, N. (2011). Crystal structure of oxygen-evolving photosystem II at a resolution of 1.9 Å. Nature *473*, 55–60.

Wang, L., Duan, L., Stewart, B., Pu, M., Liu, J., Privalov, T., and Sun, L. (2012). Toward controlling water oxidation catalysis: tunable activity of ruthenium complexes with axial imidazole/DMSO ligands. J. Am. Chem. Soc. *134*, 18868–18880.

Wasylenko, D.J., Ganesamoorthy, C., Henderson, M.A., Koivisto, B.D., Osthoff, H.D., and Berlinguette, C.P. (2010). Electronic modification of the $[Ru^{II}(tpy)(bpy)(OH_2)]^{2+}$ scaffold: effects on catalytic water oxidation. J. Am. Chem. Soc. *132*, 16094–16106.

Wilson, A.J., and Jain, P.K. (2018). Structural dynamics of the oxygen-evolving complex of Photosystem II in water-splitting action. J. Am. Chem. Soc. *140*, 5853–5859.

Xie, Y., Shaffer, D.W., and Concepcion, J.J. (2018). O-O radical coupling: from detailed mechanistic understanding to enhanced water oxidation catalysis. Inorg. Chem. *57*, 10533–10542.

Yang, B., Jiang, X., Guo, Q., Lei, T., Zhang, L.-P., Chen, B., Tung, C.-H., and Wu, L.-Z. (2016). Self-assembled amphiphilic water oxidation catalysts: control of O-O bond formation pathways by different aggregation patterns. Angew. Chem. Int. Ed. *128*, 6337–6342.

Yang, B., Yang, Q.-Q., Jiang, X., Chen, B., Tung, C.-H., and Wu, L.-Z. (2017). Tracking the Fe^{IV}(O) intermediate and O–O bond formation of a nonheme iron catalyst for water oxidation. Chem. Commun.(Camb.) *53*, 9063–9066.

Yano, J., and Yachandra, V. (2014). Mn_4Ca cluster in photosynthesis: where and how water is oxidized to dioxygen. Chem. Rev. *114*, 4175–4205.

Yu, F., Poole, D., 3rd, Mathew, S., Yan, N., Hessels, J., Orth, N., Ivanovic-Burmazovic, I., and Reek, J.N.H. (2018). Control over electrochemical water oxidation catalysis by preorganization of molecular Ruthenium catalysts in self-assembled nanospheres. Angew. Chem. Int. Ed. *57*, 11247–11251.

Zhan, S., Mårtensson, D., Purg, M., Kamerlin, S.C.L., and Ahlquist, M.S.G. (2017). Capturing the role of explicit solvent in the dimerization of Ru^{V}(bda) water oxidation catalysts. Angew.Chem. Int. Ed. *56*, 6962–6965.

Zhang, B., Li, F., Zhang, R., Ma, C., Chen, L., and Sun, L. (2016). Characterization of a trinuclear ruthenium species in catalytic water oxidation by $Ru(bda)(pic)_2$ in neutral media. Chem. Commun. *52*, 8619–8622.

Zhang, P. (2014). X-ray spectroscopy of Gold-thiolatenanoclusters. J. Phys. Chem. C *118*, 25291–25299.

Zong, R., and Thummel, R.P. (2005). A new family of Ru complexes for water oxidation. J. Am. Chem. Soc. *127*, 12802–12803.

iScience, Volume *23*

Supplemental Information

Amphiphilic Oxo-Bridged Ruthenium "Green Dimer" for Water Oxidation

Qing-Qing Yang, Xin Jiang, Bing Yang, Yang Wang, Chen-Ho Tung, and Li-Zhu Wu

NMR and ESI-MS spectrum

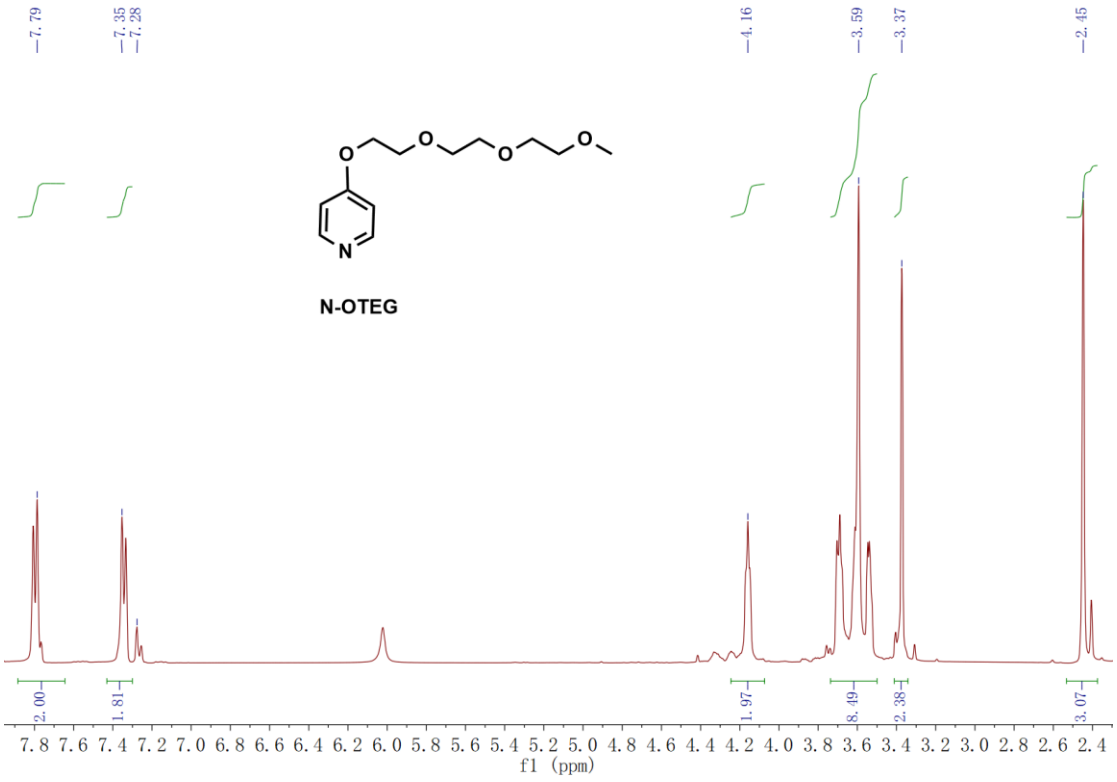

Figure S1. Related to Figure 1. ^{1}H NMR spectrum of **N-OTEG** in chloroform-*d*.

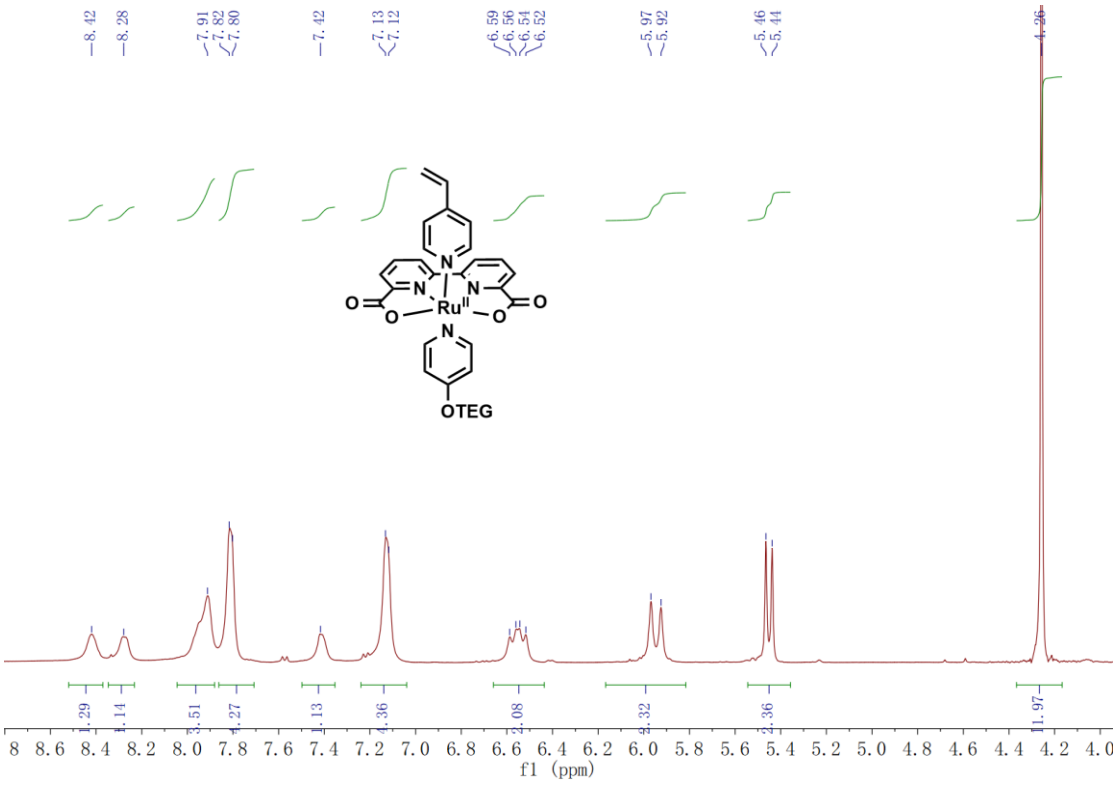

Figure S2. Related to Figure 1. ^{1}H NMR spectrum of monomer **1** in acetonitrile-d_3.

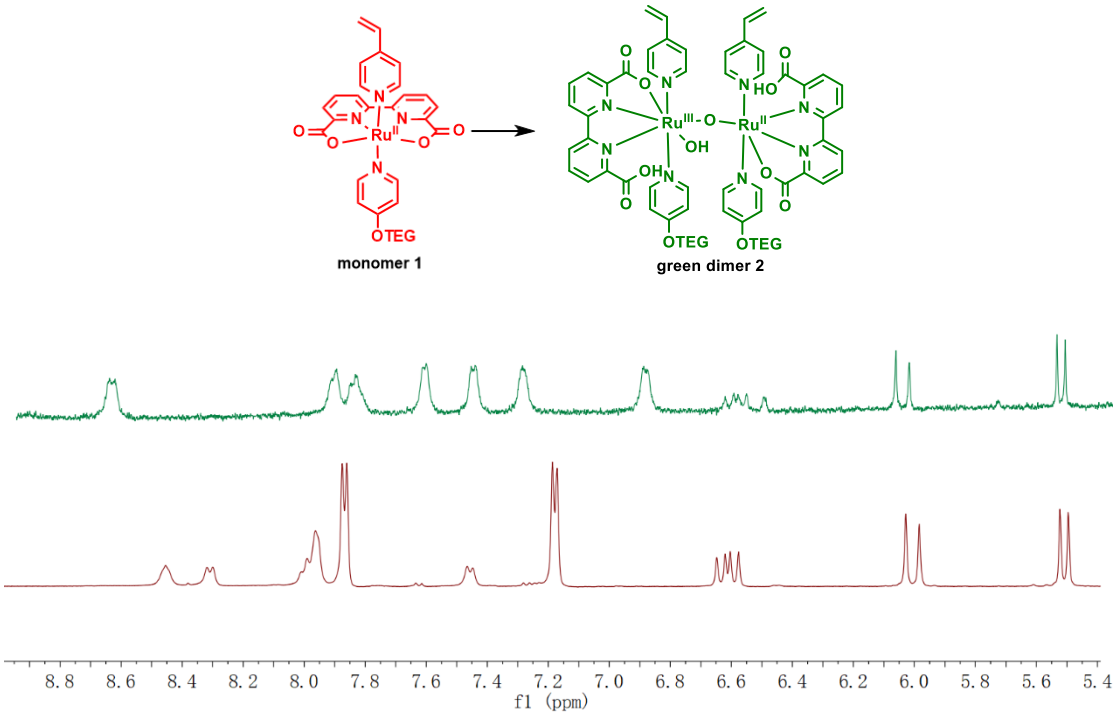

Figure S3. Related to Figure 1. ^{1}H NMR spectrum of monomer **1** (red) and dimer **2** (green) in acetonitrile-d_3.

Table S1. Related to Figure 1. The element analysis of monomer **1** and dimer **2**.

Elemental Analysis	Formulation	C (%)	H (%)	N (%)
1 (cal.)	$C_{31}H_{32}N_4O_8Ru$ (150%CH_3CN, 20% triethylamine)	54.76	5.11	10.33
1		56.01	4.06	9.63
1		56.05	4.08	9.75
2 (cal.)	$C_{62}H_{65}N_8O_{17}Ru_2$ (100%CH_3CN, 20% triethylamine)	53.66	4.87	8.83
2		54.29	4.18	9.15
2		54.51	4.10	9.34

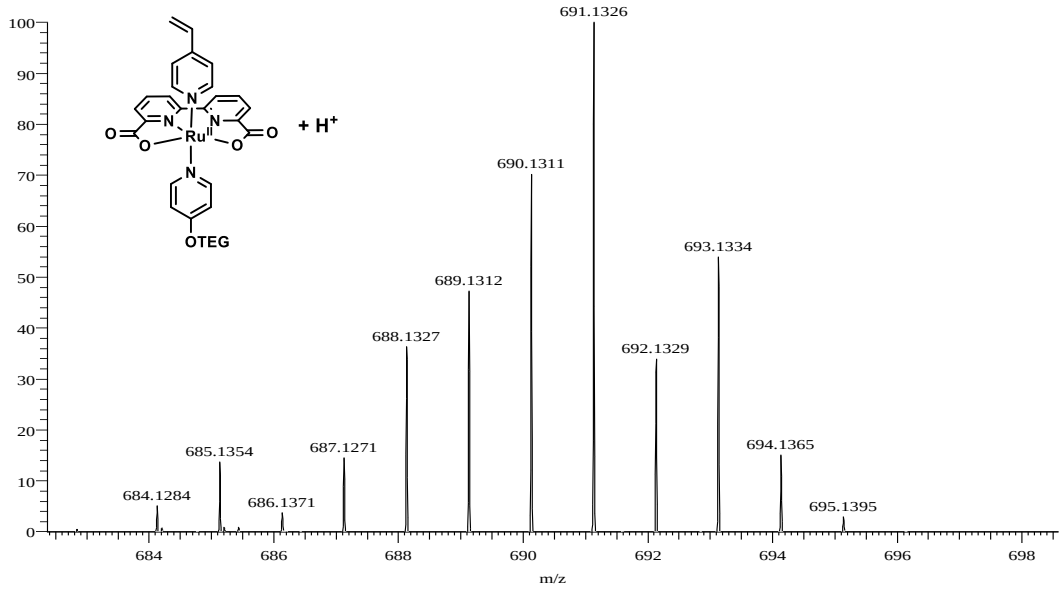

Figure S4. Related to Figure 1. ESI-MS spectrum of monomer **1** in H_2O.

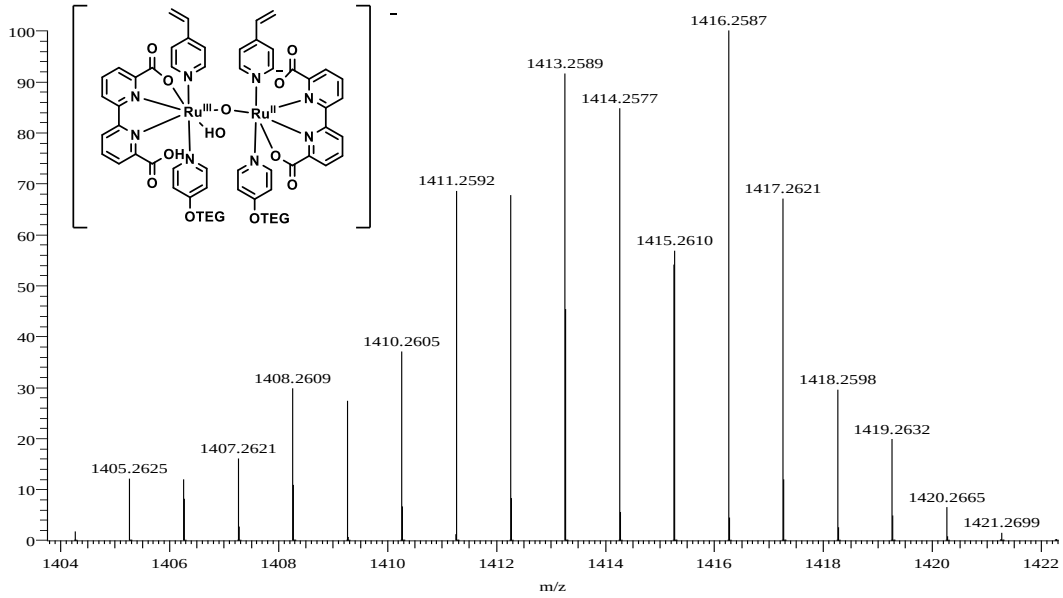

Figure S5. Related to Figure 1. Simulated mass spectra of dimer **2** in H_2O**.**

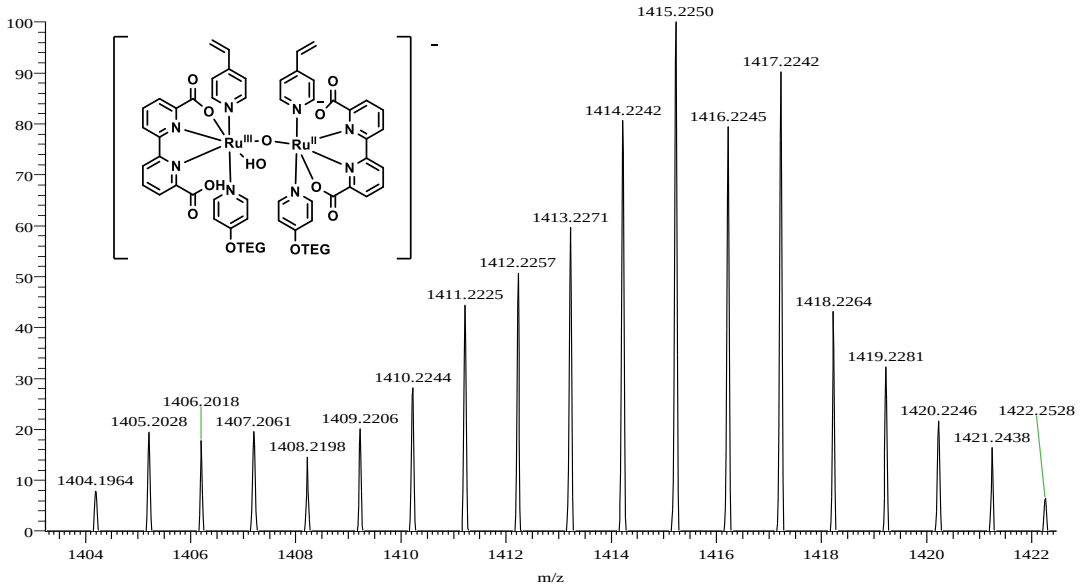

Figure S6. Related to Figure 1. ESI-MS spectrum of dimer **2** in H_2O.

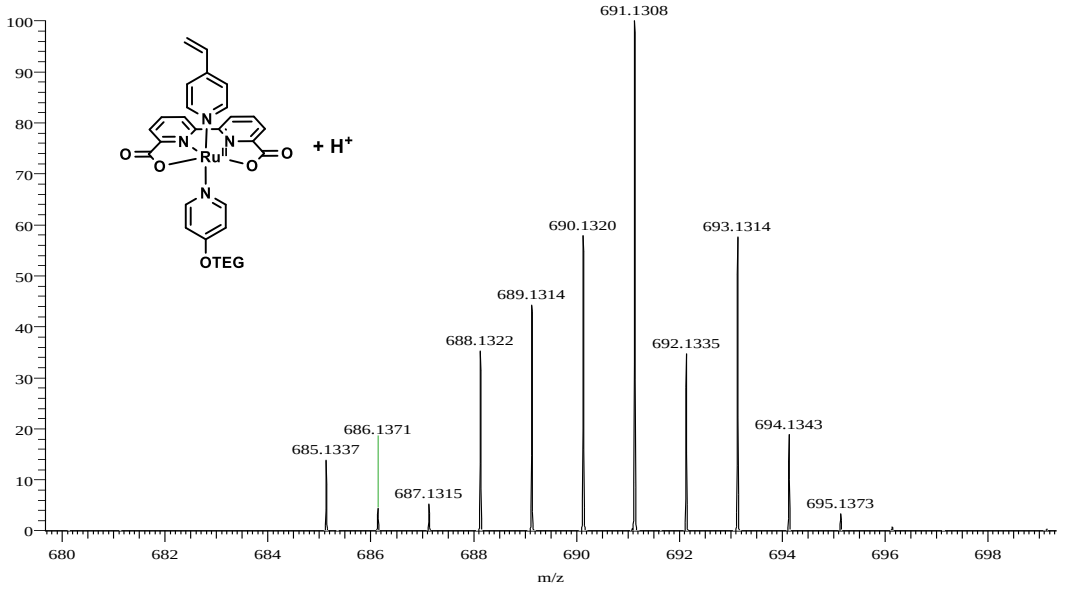

Figure S7. Related to Figure 1. ESI-MS spectrum of dimer **2** in H_2O after addition excess ascorbic acid.

Stability experiment

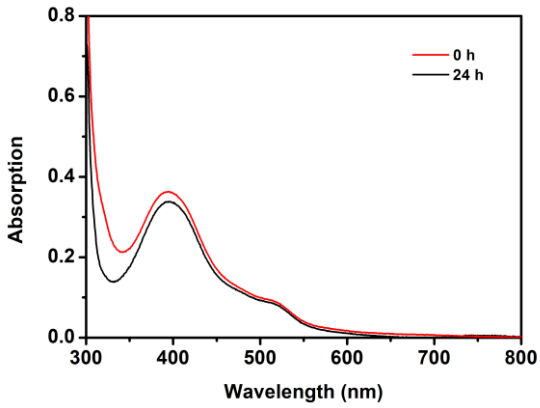

Figure S8. Related to Figure 2. The UV-vis absorption spectra of monomer **1** (2.0×10^{-5} M) in H_2O under nitrogen atmosphere.

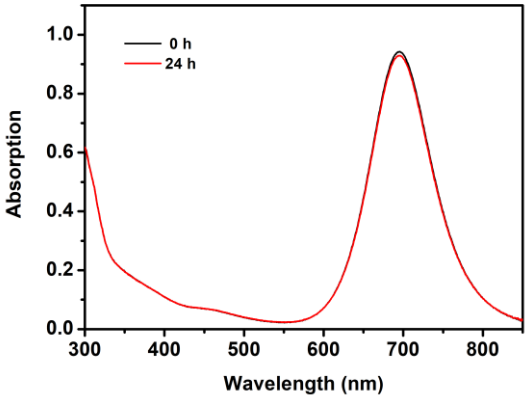

Figure S9. Related to Figure 2. The UV-vis absorption spectra of dimer **2** (1.0×10^{-5} M) in HNO_3 (pH 2.0).

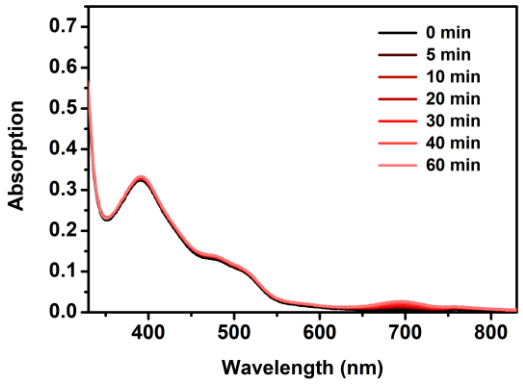

Figure S10. Related to Figure 2. The UV-vis spectral changes of monomer **1** (2.0×10^{-5} M) in H_2O

bubbled with oxygen.

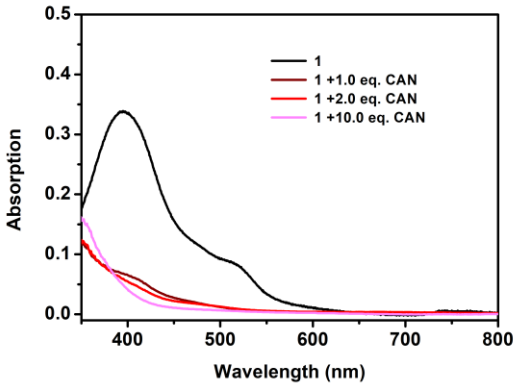

Figure S11. Related to Figure 4. The UV-vis spectral changes of monomer **1** (2.0×10^{-5} M) in aerobic aqueous solution by adding different equivalents of CAN.

UV-vis absorption spectroscopy

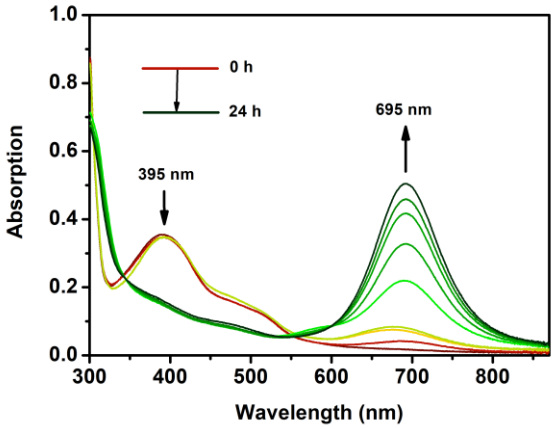

Figure S12. Related to Figure 2. Dimer **2** (1.0×10^{-5} M) was reduced by addition of 1.0 equivalent ascorbic acid to re-form **1** in H_2O. The UV-vis absorption spectra show the absorption changes of this solution upon exposure to air.

Aggregation determination

Table S2. **Related to Figure 1.** Particle size distribution of monomer **1** and dimer **2** determined by dynamic light scattering (DLS) measurements at different concentration in a solution of H_2O /CH_3CN (9/1, v/v).

	Concentration	Average size
Monomer **1**	1.0×10^{-4} M	35.9 nm
	1.0×10^{-3} M	115.9 nm
Dimer **2**	1.0×10^{-4} M	63.6 nm
	1.0×10^{-3} M	109.6 nm

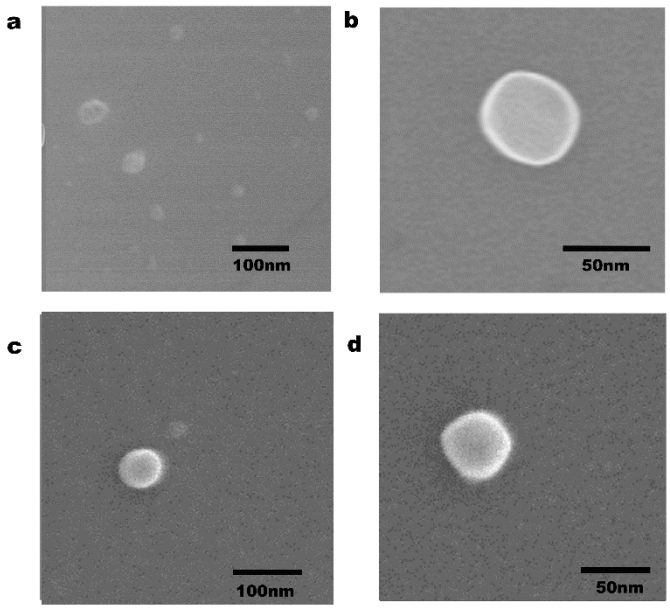

Figure S13. Related to Figure 1. Scanning electron microscope (SEM) images of dried solutions of monomer **1** (a, b) and dimer **2** (c, d) at 1.0×10^{-4} M.

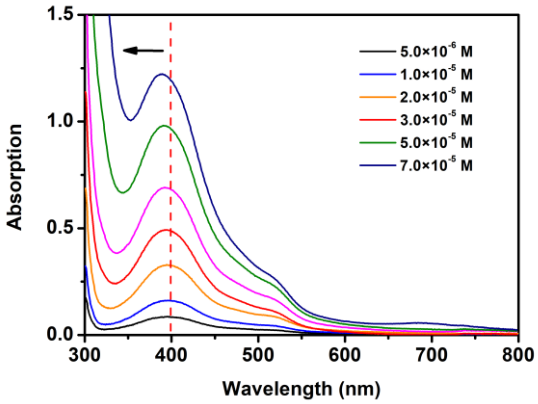

Figure S14. Related to Figure 1. UV-vis absorption changes of monomer **1** with varied concentrations in H_2O.

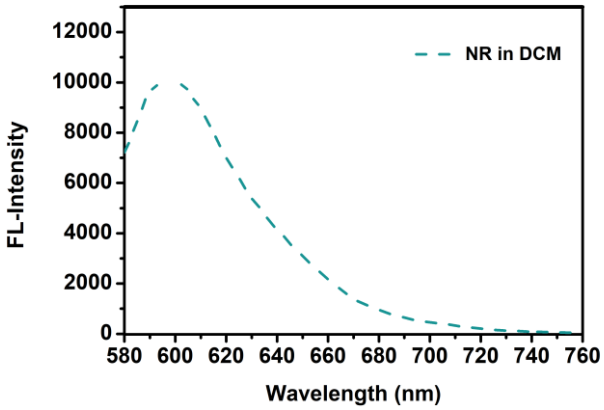

Figure S15. Related to Figure 1. The fluorescence of Nile red (NR) in DCM.

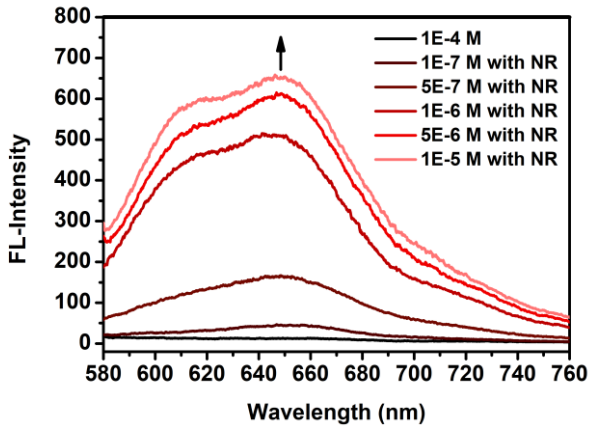

Figure S16. Related to Figure 1. The fluorescence of Nile red (NR) in the aqueous solution of monomer **1** with different concentrations. When the aggregation concentration is higher than the CAC of monomer **1**, Nile red would like to go inside of the aggregates to trigger its strong fluorescence.

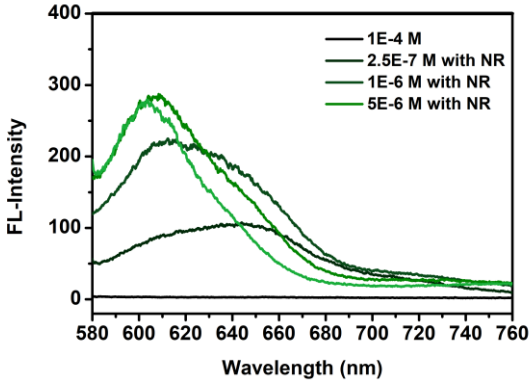

Figure S17. Related to Figure 1. The fluorescence of Nile red (NR) in the aqueous solution of dimer **2** with different concentrations.

Resonance Raman spectrum

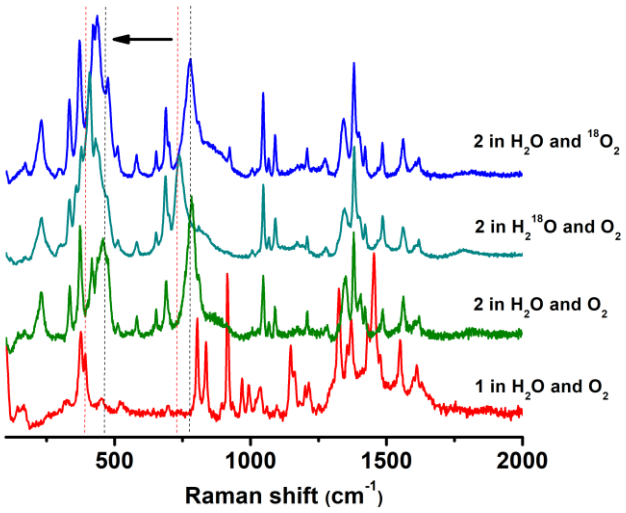

Figure S18. Related to Figure 2. Resonance Raman spectra of monomer **1** and dimer **2** in H_2O and $H_2{}^{18}O$ under O_2 or $^{18}O_2$ atmosphere with 532 nm and 633 nm excitation at room temperature. [**1**] = 1.0×10^{-3} M, [**2**] = 5.0×10^{-4} M.

Table S3. Related to Figure 2. Raman band energies and proposed assignments for dimer **2**.

Raman shift (cm^{-1})	Assignment of **2** in H_2O and O_2	Raman shift (cm^{-1})	Assignment of **2** in $H_2{}^{18}O$ and O_2	Raman shift (cm^{-1})	Assignment of **2** in H_2O and $^{18}O_2$
374	ν_{sym}(Ru–O–Ru)	359	ν_{sym}(Ru–^{18}O–Ru)	369	ν_{sym}(Ru–^{18}O–Ru)
462	ν_{sym}(Ru–O–Ru) + 88	409	ν_{sym}(Ru–^{18}O–Ru) + 50	430	ν_{sym}(Ru–^{18}O–Ru) + 61
785	ν_{sym}(Ru–O–Ru) + 411	741	ν_{sym}(Ru–^{18}O–Ru) + 382	771	ν_{sym}(Ru–^{18}O–Ru) + 402

X-ray Absorption Spectroscopy (XAS) spectrum

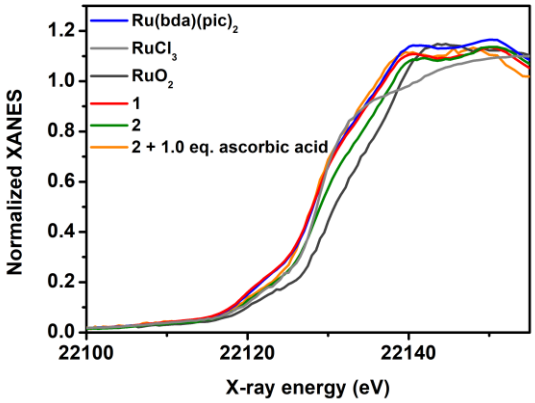

Figure S19. Related to Figure 3. Normalized Ru K-edge XANES of $Ru(bda)(pic)_2$, $RuCl_3$, RuO_2, monomer **1**, dimer **2** and dimer **2** reduced by 1.0 equivalent ascorbic acid VC (relative to the concentration of **2**)

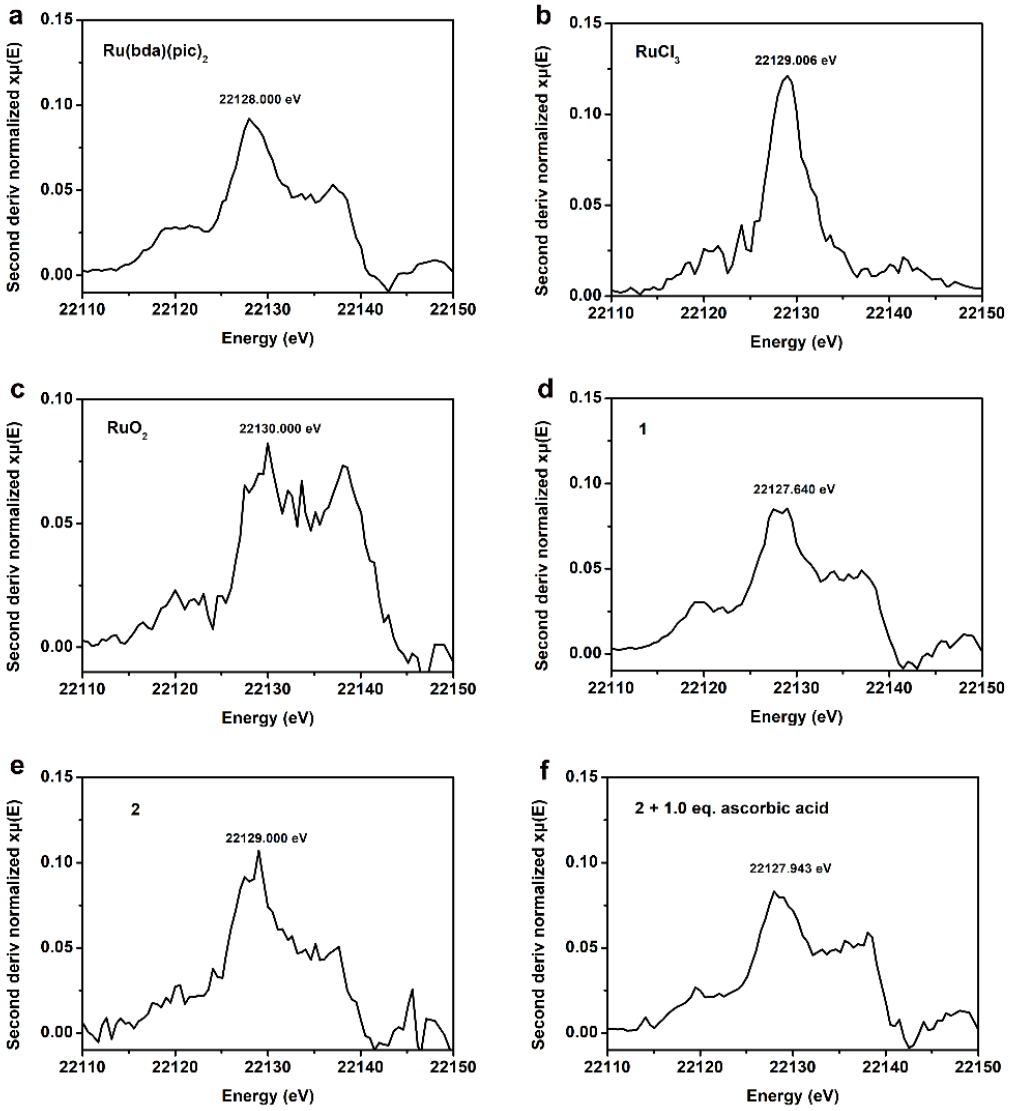

Figure S20. Related to Figure 3. The K-edge XANES derivatives of $Ru(bda)(pic)_2$, $RuCl_3$, RuO_2, monomer **1**, dimer **2** and dimer **2** reduced by 1.0 eq. ascorbic acid (relative to the concentration of **2**) were showed as a-f.

Table S4. Related to Figure 3. Comparison of XANES energy for reference complexes

Sample	Energy at Normalized fluorescence (eV)
$Ru(bda)(pic)_2$	22128.0
$RuCl_3$	22129.0
RuO_2	22130.0
Monomer **1**	22127.6
Dimer **2**	22129.0
Dimer **2**+1.0 eq ascorbic acid	22127.9

X-ray absorption fine structure (EXAFS) spectrum

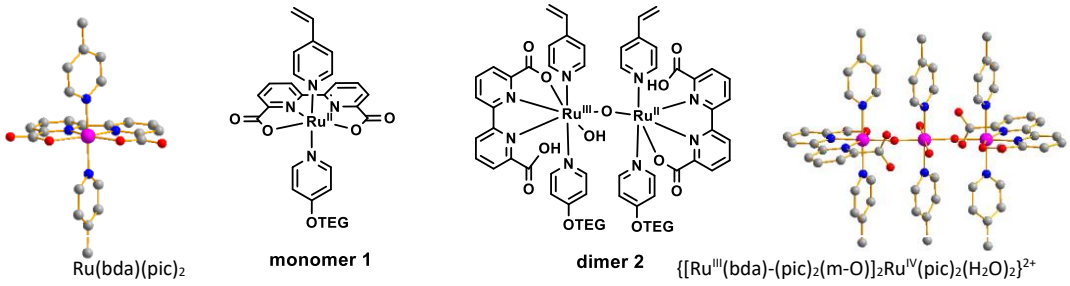

Figure S21. Related to Figure 3. The crystallographic stuctures of $Ru(bda)(pic)_2$ (left) and $\{[Ru^{III}(bda)\text{-}(pic)_2(m\text{-}O)]_2Ru^{IV}(pic)_2(H_2O)_2\}^{2+}$ (right) are shown blow (Ru atoms are pink, O atoms are red, N atoms are blue, C atoms are grey and H atoms have been omitted for clarity).

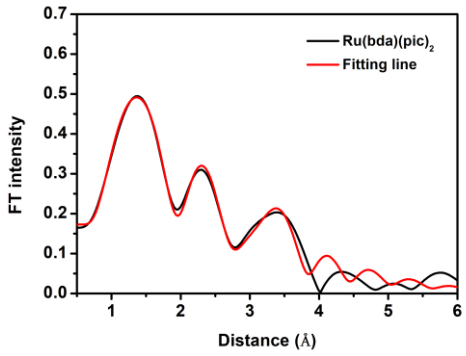

Figure S22. Related to Figure 3. Corresponding k^3-weighted Fourier transform (FT) of Ru EXAFS of $Ru(bda)(pic)_2$ powder by using the crystallographic data of $Ru(bda)(pic)_2$ for fitting analysis.

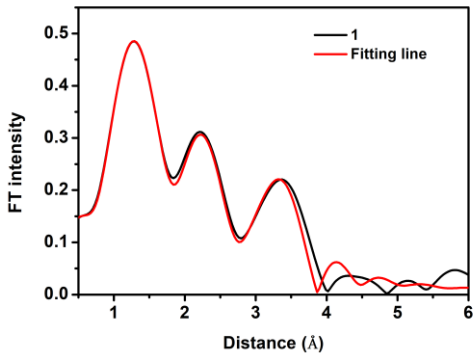

Figure S23. Related to Figure 3. Corresponding k^3-weighted Fourier transform (FT) of Ru EXAFS of monomer **1** (powder) by using the crystallographic data of $Ru(bda)(pic)_2$ for fitting analysis.

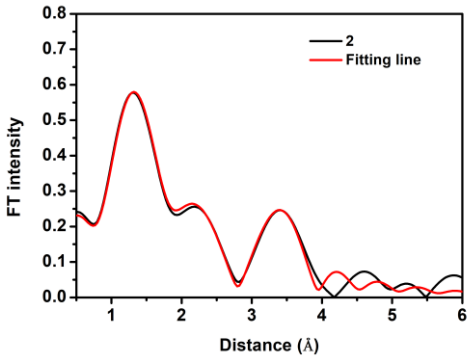

Figure S24. Related to Figure 3. Corresponding k^3-weighted Fourier transform (FT) of Ru EXAFS of dimer **2** (5 mM) by using the crystallographic data of $\{[Ru^{III}(bda)\text{-}(pic)_2(m\text{-}O)]_2Ru^{IV}(pic)_2(H_2O)_2\}^{2+}$ for fitting analysis.

Table S5. Related to Figure 3. EXAFS fits for $Ru(bda)(pic)_2$, monomer **1** and dimer **2**

	Scattering atoms, N	Coordination distance of Reference (Å)	Fitting distance of XAR (Å)	$\sigma^2(\times10^{-3})$	E_0	R-factor $(\times10^{-3})$	Reduced Chi-square
Monomer **1**	Ru-N, 4	1.91410	1.91426	10.78	-2.0	2.4061	264.14
	Ru-O, 2	2.17200	2.06219	0. 80			
	Ru-C, 10	2.81340	2.83606	8.84			
	Ru-C, 10	4.16810	4.15853	1.67			
$Ru(bda)(pic)_2$	Ru-N	1.94970	1.73215	33.92	12.29	3.5507	182.569
	Ru-O, 2	2.17200	2.07278	6.67			
	Ru-C, 10	2.81340	2.95869	11.71			
	Ru-C, 10	4.16810	3.80433	30.30			
Dimer **2**	Ru-N	2.10120	1.96669	6.56	0.756	5.9923	1.17
	Ru-O, 3	1.90340	2.13645	7.15			
	Ru-C, 10	2.99480	2.89972	18.01			
	Ru-C, 10	4.16810	4.16992	3.04			
	Ru-O-Ru, 1	3.69830	3.51225	3.51			

σ^2 is the Debye-Waller factor; Amplitude reduction factor (S_0^2) was set; E_0 is energy shift; Errors were estimated as R - ± 1%; The crystallographic data of $Ru(bda)(pic)_2$ and $\{[Ru^{III}(bda)\text{-}(pic)_2(m\text{-}O)]_2Ru^{IV}(pic)_2(H_2O)_2\}^{2+}$ were used to fit the EXAFS data.

Oxygen evolution measurements

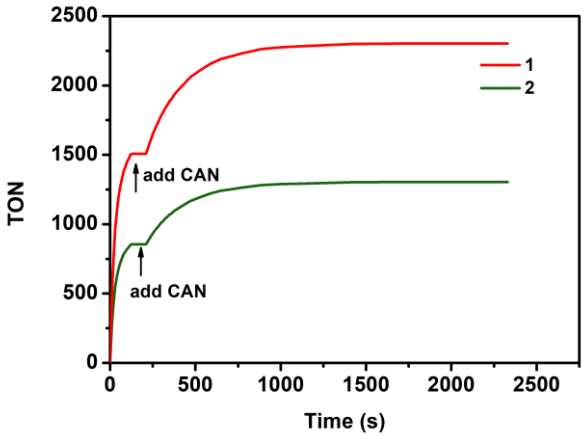

Figure S25. Related to Figure 4. Kinetic plots of oxygen formation by monomer **1** and dimer **2** vs time using the water displacement method. Conditions: 4.0 mL aqueous solution containing [**1, 2**] = 7.0×10^{-5} M, [CAN] = 0.5 M.

Table S6. Related to Figure 4. ^{18}O labelling experiment by GC-MS analysis of monomer **1** and dimer **2** (1.0×10^{-3} M) with CAN (1.0×10^{-2} M in 97% $H_2{}^{18}O$) at 298 K. (Theoretical values were calculated by assuming that evolved oxygen comes only from 97% $H_2{}^{18}O$.)

	Relative abundance, %		
	$^{16}O_2$	$^{16}O^{18}O$	$^{18}O_2$
Theoretical	0.09	5.82	94.09
Monomer **1**	3.00	7.83	89.17
Dimer **2**	2.68	6.08	91.24

Electron paramagnetic resonance (EPR) experiments

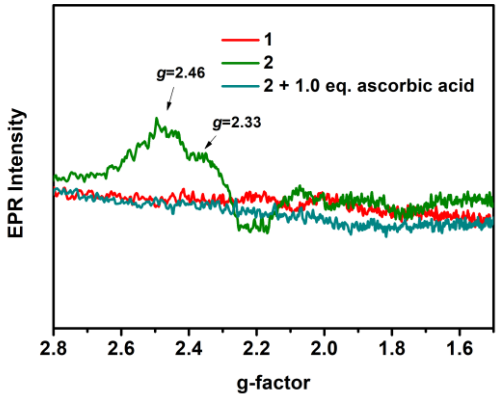

Figure S26. Related to Figure 3. X-Band EPR spectra of 1.0×10^{-3} M solutions of monomer **1** (black), dimer **2** (blue) and mixture (green) generated by adding 1.0 equiv. of ascorbic acid to aqueous solution of dimer **2**.

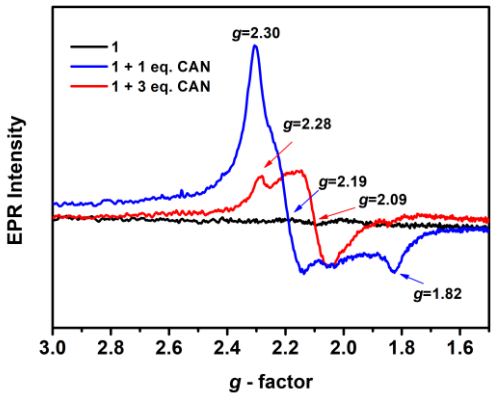

Figure S27. Related to Figure 5. X-Band EPR spectra of 1.0×10^{-3} M solutions of monomer **1** by adding different equivalents of CAN at 90 K.

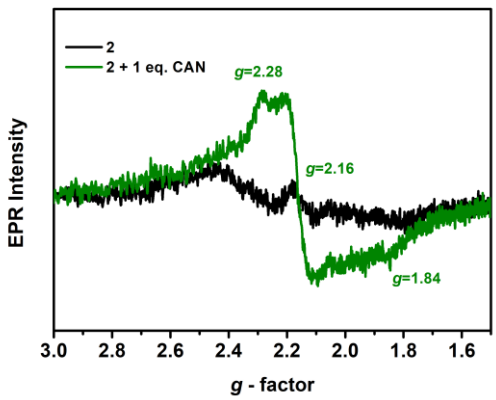

Figure S28. Related to Figure 5. X-Band EPR spectra of 1.0×10^{-3} M solutions of dimer **2** by adding 1.0

equivalent of CAN at 90 K.

Electrochemical measurements

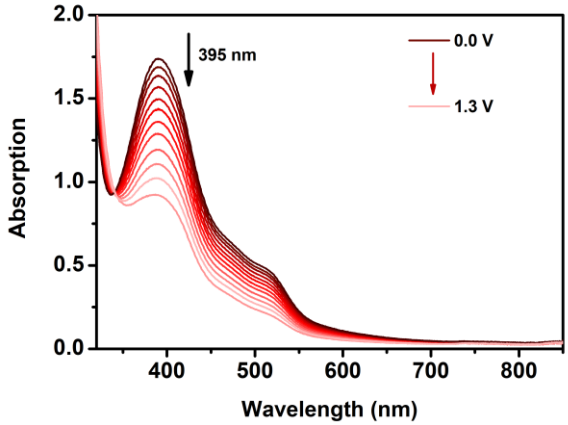

Figure S29. Related to Figure 5. The spectroelectrochemistry of monomer **1** (1.0×10^{-4} M) in 0.1 M HNO_3 (V_{H2O}/V_{CH3CN} = 3/1) with the bias increasing from 0 to 1.3 V vs. SCE. Conditions of (a) and (b): glassy carbon as working electrode, Pt wire as auxiliary electrode, and saturated calomel electrode as reference electrode.

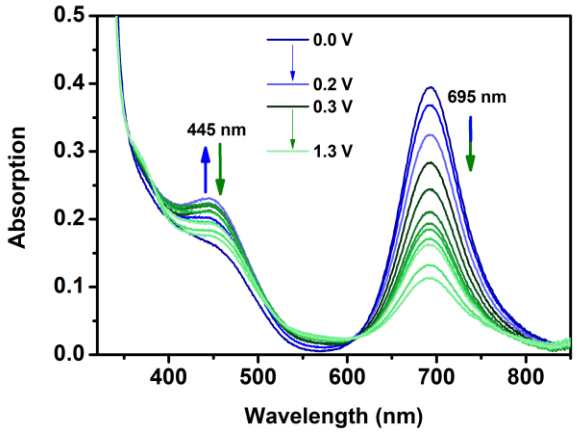

Figure S30. Related to Figure 5. The spectroelectrochemistry of dimer **2** (5.0×10^{-6} M) in 0.1 M HNO_3 with the bias increasing from 0 to 1.3 V vs. SCE. Conditions of (a) and (b): glassy carbon as working electrode, Pt wire as auxiliary electrode, and saturated calomel electrode as reference electrode.

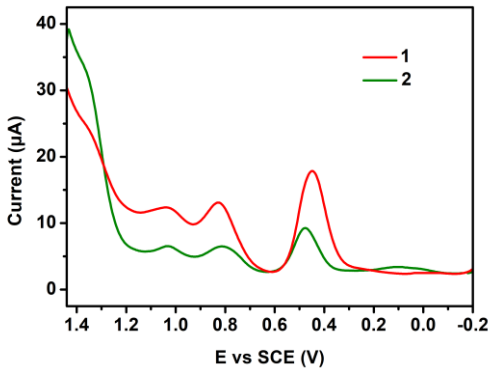

Figure S31. Related to Figure 5. Differential pulse voltammograms (DPV) of monomer **1** and dimer **2** in H_2O with 0.1 M Na_2SO_4, pH= 2.0 (0.1 M HNO_3-NaOH to adjust the pH values), glassy carbon as working electrode, Pt wire as auxiliary electrode, and saturated calomel electrode as reference electrode.

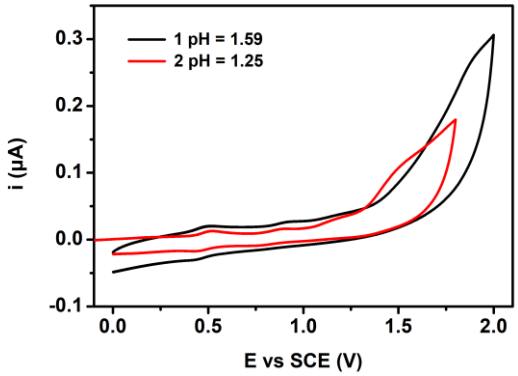

Figure S32. Related to Figure 5. The cyclic voltammetry (CV) of complex monomer **1** and dimer **2** in H_2O with 0.1 M HNO_3 and 0.1 M Na_2SO_4, glassy carbon as working electrode, Pt wire as auxiliary electrode, and saturated calomel electrode as reference electrode.

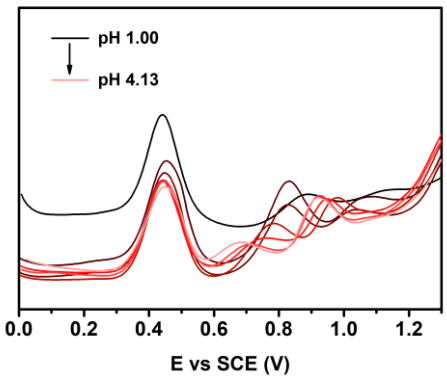

Figure S33. Related to Figure 5. DPV of monomer **1** in H_2O with 0.1 M Na_2SO_4, pH = 1-5 (0.1 M HNO_3-NaOH to adjust the pH values), glassy carbon as working electrode, Pt wire as auxiliary electrode, and saturated calomel electrode as reference electrode.

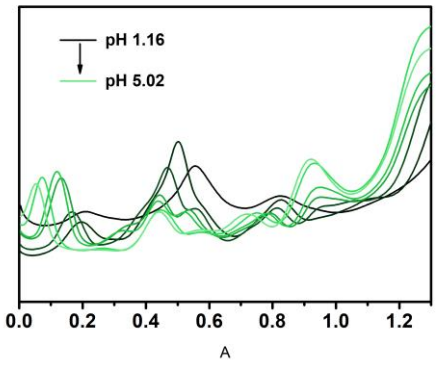

Figure S34. Related to Figure 5. DPV of dimer **2** in H_2O with 0.1 M Na_2SO_4, pH = 1-5 (0.1 M HNO_3-NaOH to adjust the pH values), glassy carbon as working electrode, Pt wire as auxiliary electrode, and saturated calomel electrode as reference electrode.

Transparent Methods

Materials and Methods

NMR spectra were recorded with a Bruker Avance DPX 400 MHz instrument with tetramethylsilane (TMS) as an internal standard. HRMS (ESI) spectra were measured with a Thermo Fisher Q-Exactive Mass Spectrometer. The elemental analysis of C, H, N was obtained by Flash EA 1112 at room temperature. The sample of **1** and **2** for elemental analysis have been dried at 80℃ for 12 hours. UV-Vis spectral data were performed by Shimadzu UV-1601PC UV-Visible spectrophotometer. Raman spectra were determined on an inVia-Reflex with excitation at 532 nm and 633 nm at 90 K. The EPR experiments were carried out on the Bruker E500 variable temperature magnetic resonance instrument at 90 K. X-Ray absorption spectroscopic (XAS) data were obtained at Beam line BL14W1 of the Shanghai Synchrotron Radiation Facility (SSRF). DPV and CV experiments were performed on a one-compartment three electrode cell. The pH values were measured on ORION Model 828. Glassy carbon disk electrodes were used as working, platinum wire as auxiliary and a SCE as reference electrode. Complexes were dissolved in water containing Na_2SO_4 (0.1 M) as electrolyte. All potentials reported herein were converted to their corresponding values versus SCE. Oxygen evolution was recorded with a Hansatech Oxygraph or through the method of displacement of water using an upside-down burette.

X-ray Absorption Spectroscopy (XAS) Methods.

X-ray absorption spectra were collected at the Shanghai Synchrotron Radiation Facility. The radiation was monochromatized by a Si(311) crystal monochromator. The intensity of the X-rays were monitored by three ion chambers (I_0, I_1 and I_2) filled with 50% nitrogen and 50% argon and placed before the sample (I_0) and after the sample (I_1 and I_2). The samples were kept at 298 K with ambient pressure. The standard samples of Ru^0, $Ru(bda)(pic)_2$, $RuCl_3$, RuO_2 were recorded as transmission model and the other solid and liquid samples were fluorescence excitation spectra. Ru XAS energy was calibrated by the first maxima in the derivative of the ruthenium metal X-ray and no damage was observed scan after scan to any samples.

Absorption Near Edge Structure spectrum.

Athena software was used for data processing. The energy scale for each scan was normalized using Ruthenium foil. Data in energy space were pre-edge corrected, normalized, and background corrected. The processed data were next converted to the photoelectron wave vector (k) space and weighted by k^3.

The electron wave number is defined as $k = [2m(E - E_0)/h^2]^{1/2}$, E_0 is the energy origin or the threshold energy. K-space data were truncated near the zero crossings k = 3 to 8.5 Å^{-1} for samples, in Ru EXAFS before Fourier transformation. The k-space data were transferred into the Artemis Software for curve fitting. The Fourier peaks were isolated separately, grouped together, or the entire (unfiltered) spectrum was used to fit the data. The individual Fourier peaks were isolated by applying a Hanning window. Curve fitting was performed using *ab initio*-calculated phases and amplitudes from the FEFF6 program from the University of Washington. *Ab initio*-calculated phases and amplitudes were used in the EXAFS equation

$$\chi(k) = {S_0}^2 \sum_j \frac{N_j}{k{R_j}^2} f_{eff_j}(\pi, k, R_j) e^{-2\sigma_j{}^2 k^2} e^{-2R_j/\lambda_j(k)} sin(2kR_j + \phi_{ij}(k)) \qquad (1)$$

where N_j is the number of atoms in the *j*th shell; R_j is the mean distance between the absorbing atom and the atoms in the *j*th shell; $f_{eff_j}(\pi, k, R_j)$ is the *ab initio* amplitude function for shell *j*, and the Debye-Waller term $e^{-2\sigma_j{}^2 k^2}$ accounts for damping due to static and thermal disorder in absorber-back scattered distances. The mean free path term $e^{-2R_j/\lambda_j(k)}$ reflects losses due to inelastic scattering, where $\lambda_j(k)$, is the electron mean free path. The oscillations in the EXAFS spectrum are reflected in the sinusoidal term $sin(2kR_j + \phi_{ij}(k))$, where $\phi_{ij}(k)$ is the *ab initio* phase function for shell *j*. This sinusoidal term shows the direct relation between the frequency of the EXAFS oscillations in k-space and the absorber-back scattered distance. $S_0{}^2$ is an amplitude reduction factor.

The EXAFS equation (1) was used to fit the experimental Fourier isolated data (q-space) as well as unfiltered data (k-space) and Fourier transformed data (R-space) using *N*, $S_0{}^2$, E_0, *R*, and σ^2 as variable parameters (Table S5). *N* refers to the number of coordination atoms surrounding Ru for each shell. The quality of fit was evaluated by R-factor and the reduced χ^2 value. R-factor less than 1% denotes that the fit is good enough. The reduced χ^2 value is used to compare fits as more absorber-backscatter shells are included to fit the data. A smaller reduced χ^2 value implies a better fit. Similar results were obtained from fits done in k, q, and R-spaces. To determine the Ru-O, Ru-N and Ru-C bonds, the crystallographic data of Ru(bda)(pic)$_2$ was used in FEFF to fit the XANES of Ru(bda)(pic)$_2$ and monomer **1**. To determine the Ru-O-Ru bond, a model accounting for backscattering amplitude and phase shift of the Ru-O-Ru three atom system reported by Sakai (*Chem. Commun.* **2016**, *52*, 8018-8021) was created for dimer **2**.

Procedures for Resonance Raman experiments

The sample of dimer **2** (1.0×10^{-3} M) was prepared by the treatment of monomer **1** (2.0×10^{-3} M) with O_2 in H_2O. All the solution was pumped with Ar for 40 min. The excitation at 532 nm was chosen to test monomer **1** and 633 nm for dimer **2**, which are close to the maximum absorption, respectively. The isotopologue of dimer **2** was prepared by the treatment of monomer **1** (2.0×10^{-3} M) with $^{18}O_2$ in $H_2{}^{16}O$ or $^{16}O_2$ in $H_2{}^{18}O$. The $^{18}O_2$ gas was obtained from the water oxidation reaction by **1** with CAN in $H_2{}^{18}O$.

Procedures for EPR experiments

The sample of **1** and **2** (1.0×10^{-3} M) in H_2O was prepared. All the solution was pumped with Ar for 40 min. For detection of the intermediates, the solution of **1** or **2** was added into an EPR tube and then the corresponding equivalents of CAN was added immediately. The mixed solution was frozen within 5 seconds in the sample chamber at 90 K. The EPR spectrum was recorded using 1500-Hz field modulation.

Procedures for Spectroelectrochemical Study

Spectroelectrochemical experiments were performed in Shimadzu UV-1601PC UV-Visible spectrophotometer in combination with a home-built sample compartment consisting of a quartz cell with an open window and an adjustable three electrodes (5 mm glassy carbon electrode, 1 mm platinum counter and Ag/AgCl reference electrode). The added bias was controlled by the constant-potential electrolysis mode for 300 s.

Procedures for O_2 evolution measurements

The water displacement and Clark oxygen electrode were used to detect the released O_2. The 4 mL of monomer **1** or **2** (7.0×10^{-7} M), and CAN (0.5 M) in water was sealed in a 10 mL test tube. The large quantities of evolved oxygen were passed into a graduated tube which was full of water. The O_2 gas would displace the water and the volume of evolved oxygen was recorded. The kinetic isotope effect experiments were carried out in an Oxygraph Plus System of Hansatech Instruments Ltd. (Clark-type oxygen electrode). 2.0 mL of a prepared CAN solution (1.0×10^{-3} M, pH = 2 in water) was placed in the Clark electrode reaction chamber. After the baseline of the measurement was constant, 10-50 μL of the catalyst solution (varying concentrations) in water were added. During the measurement the reaction temperature was kept constant at 25 °C. The ^{18}O labelling experiments were performed under ambient conditions in a sealed test tube. CAN (1.0×10^{-2} M) was dissolved in 1 mL of 97% $H_2{}^{18}O$ and the catalysts (1.0×10^{-3} M) was injected to it through a septum via a Hamilton styringe. After the gas evolution had ceased for 20 min, 200 μL of the gas were taken out by a gas tight Hamilton syringe and injected into the

gas chromatograph GC-2030 from Shimadzu (argon as carrier gas) with a mass spectrometry.

Synthesis of monomer 1 and dimer 2

$Ru(DMSO)_4Cl_2$ were prepared according to the literature methods. All other reagents for synthesis in this work were obtained commercially. Deionized water with resistivity of 18.2 MΩ·cm (Barnstead 3750) was used.

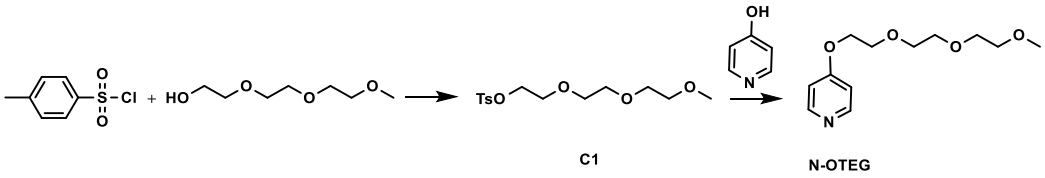

Synthesis of complex **N-OTEG** (**TEG** = $O(CH_2CH_2O)_3CH_3$):

0.7 g (3.65 mmol, 1.2 equiv.) of 4-toluene sulfonyl chloride, 0.5 g (3.04 mmol, 1.0 equiv.) of triethylene glycol monomethyl ether and 0.5 mL (3.65 mmol, 1.2 equiv.) of triethylamine were suspended in 20 mL of CH_2Cl_2. The suspension was stirred under room temperature for 5 h. Purification was performed via column chromatography on silica gel with CH_2Cl_2/CH_3OH (10:1/v:v) as eluent to give a oil of 2-[2-(2-methoxyethoxy)ethoxy]ethoxy benzenesulfonate (**C1**) (0.81 g, 84%). 57 mg (0.60 mmol, 1.0 equiv.) of 4-hydroxypyridine, 229 mg of (0.72 mmol, 1.2 equiv.) of **C1** and 250 mg (1.8 mmol, 3.0 equiv.) of K_2CO_3 were suspended in 20 mL of DMF. The suspension was stirred under reflux for 24 h. The residue was purified by column chromatography on silica gel with CH_2Cl_2/CH_3OH (10:1/v:v) resluting 140 mg of **N-OTEG** (80%). ^{1}H NMR (400 MHz, Chloroform-*d*) δ 7.79 (s, 2H), 7.35 (s, 2H), 4.16 (s, 2H), 3.59 (s, 8H), 3.37 (s, 2H), 2.45 (s, 3H).

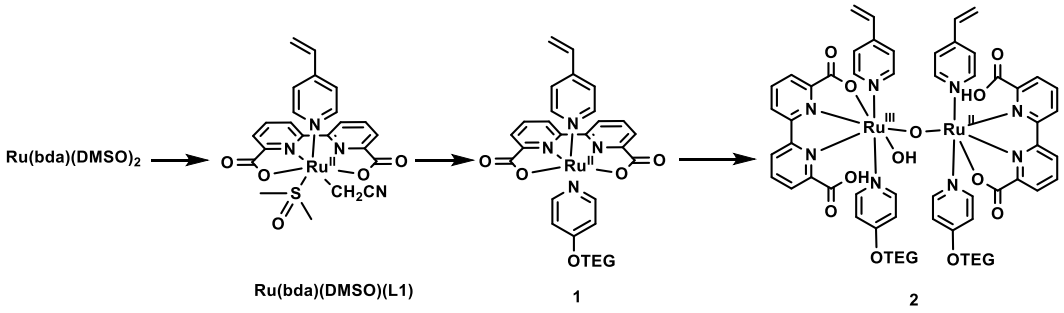

Under argon atmosphere, 162.8 mg (0.226 mmol, 1.0 equiv.) of $Ru(bda)(DMSO)_2$ and 34.2 mg vinylpyridine (**L1**) (0.326 mmol, 1.4 equiv.) were suspended in 10 mL of CH_3CN. The suspension was stirred under reflux for 1 h. After the solution cooled to room temperature, the mixture were filtered to get the residue of Ru(bda)(DMSO)(**L1**) (105 mg, 82%), which was washed with acetonitrile and ether.

Under argon atmosphere, 88.7 mg (0.157 mmol, 1.0 equiv.) of Ru(bda)(DMSO)(**L1**) and 37.3 mg (0.157 mmol, 1.0 equiv.) of **N-OTEG** were suspended in 10 mL of CH_3OH. The suspension was stirred under reflux for 12 h. Purification was performed via column chromatography on silica gel with CH_2Cl_2/CH_3OH (20:1/v:v) as eluent, a red solid of **1** (43 mg, 40%) was obtained. ^1H NMR (400 MHz, Acetonitrile-d_3) δ 8.42 (s, 1H), 8.28 (s, 1H), 7.91 (s, 3H), 7.81 (d, J = 5.8 Hz, 4H), 7.42 (s, 1H), 7.12 (d, J = 5.9 Hz, 4H), 6.55 (dd, J = 17.5, 10.9 Hz, 2H), 5.95 (d, J = 17.5 Hz, 2H), 5.45 (d, J = 10.9 Hz, 2H), 4.26 (s, 12H). The aqueous solution ofmonomer **1** was reflexed with water under air for 24 h. The solvent was removed and was purified by column chromatography on silica gel with CH_3OH/H_2O (10:1/v:v) under vacuum to give a green solid of dimer **2**.